Ultrahigh Temperature Metamorphism: testing Models for Collision vs. Extension

Thesis submitted in accordance with the requirements of the University of Adelaide for an Honours Degree in Geology

Matilda Mary Greenslade

November 2015

THE UNIVERSITY of ADELAIDE

ULTRAHIGH TEMPERATURE METAMORPHISM: TESTING MODELS FOR COLLISION VS. EXTENSION

METAMORPHISM: COLLISION VS. EXTENSION

ABSTRACT

The Warumpi Province has been interpreted to be exotic and accreted to the Northern Australian Craton (NAC) during the Liebig Orogeny at c.1640Ma. However, phase equilibria modelling of melt-deficient, Mg-Al rich granulite facies rocks at Hill 830, in the Mount Liebig area show contradictory evidence of a decompressional pressure-temperature path and a high metamorphic gradient of 90°Ckbar^{-}. This interpretation in conjunction with abundant c. 1780- 1740Ma and c. 1640Ma magmatism in the southern Aileron and Warumpi Provinces, indicate that the tectonic regime at c. 1640Ma may instead be a south-migrating, extensional scenario, compared to the previously accepted collisonal regime; speculating that the Warumpi Province is not 'exotic' to the NAC.

KEYWORDS

Ultrahigh temperature metamorphism, Warumpi Province, Liebig Orogeny, Grenvillian-aged reworking, Phase forward equilibria modelling, Pseudosection, U-Pb monazite geochronology

TABLE OF CONTENTS

LIST OF FIGURES AND TABLES

INTRODUCTION

The tectonic evolution of the southern margin of the North Australian Craton (NAC)—including the Warumpi Province—in central Australia is characterised by a prolonged and complex history spanning the period c. 1860–350 Ma (Claoue-Long and Edgoose 2008; Collins and Shaw 1995; Scrimgeour et al. 2005a; Scrimgeour et al. 2005b; Raimondo et al. 2011). The region is characterised by numerous periods of sedimentation interspersed with periods of (usually) voluminous magmatism and high thermal-gradient metamorphism (Buick et al. 2011; Claoue-Long and Hoatson 2005; Morrissey et al. 2011; Wong et al. 2015/in press). The long-standing view is that subduction-related collisional processes dominate the tectonic evolution of the region (Scrimgeour 2003; Scrimgeour et al. 2005b; Selway et al. 2009). However, more recent work has suggested that extensional tectonic processes – also subduction-related – may play an important role in the evolution of the NAC, including the Warumpi Province (e.g. Tucker et al. 2015; Walsh et al. 2015/in press; Wong et al. 2015/in press). The timeline of c. 1640 Ma is a comparatively recently recognised regional timeline (Scrimgeour et al. 2005b) in the NAC–Warumpi Province and was interpreted by Scrimgeour et al. (2005b) to record the collisional accretion of the exotic Warumpi Province with the NAC. The collisional interpretation for the tectonic setting rests heavily on two criteria: 1) that the Warumpi Province is exotic to the NAC; and 2) the thermobarometric (or pressure–temperature, *P*–*T*) results presented by Scrimgeour et al. (2005). With more recent geochronological and reconnaissance Hf isotopic work (e.g. Anderson 2015; Fields 2012; Lawson-Wyatt 2012; Wong et al. 2015/in press) the Warumpi Province and NAC and have been shown to have a shared Palaeoproterozoic history, both containing c. 1780–1750 Ma granitoids and overlapping, comparatively

juvenile Hf isotopic signatures for those c. 1750 Ma granitoids (Anderson 2015). Therefore, the Warumpi Province does not appear to be exotic to the Warumpi Province. The *P–T* results of Scrimgeour et al. (2005b) are yet to be scrutinised, and as such, form the basis of this study. The *P–T* results were obtained from unusual high-Mg–Al orthopyroxene-bearing granulites in a spatially restricted portion of the Warumpi Province.

In this study detailed petrography will be undertaken to constrain the peak metamorphic assemblage of the Mg–Al-rich granulites. With the mineralogical framework provided by petrography and field outcrop observations I will robustly constrain the *P–T* conditions using calculated phase diagrams (*P–T* pseudosections). Monazite geochronology will be used to place the petrology and *P–T* estimates into a time-integrated framework. These results will shed light on the thermal gradients and together with field geological observations will allow for a critical appraisal of the interpreted tectonic regime for the southern NAC and Warumpi Province at c. 1640 Ma.

Figure 1: Simplified geological map showing the location of the Warumpi Province at the southern margin of the North Australian Craton, known locally as the Aileron Province of the Arunta Region). The study area is boxed and is presented in more detail in Figure 2. Adapted from Wong et al. (2015/in press)

GEOLOGICAL SETTING AND BACKGROUND TO EXISTING THERMOBAROMETRY

Regional Geological Setting

The Arunta Region is the southernmost outcropping part of the Northern Australia Craton. The Arunta Region was subdivided into three tectonic provinces based on lithologies and protolith ages (Buick et al. 2001; Scrimgeour 2004; Scrimgeour et al. 2005b); the eastern Neoproterozoic to Cambrian Irindina Province, northern Aileron Province and southern Warumpi Province.

The protracted tectonic history of the southern NAC and Warumpi Province includes, in order, the following events, for which age data is summarised in Table 1. Voluminous magmatism was produced in the Arunta Region during the c. 1780–1740 Ma Yambah–Inkamulla events, with magmatism showing a general younging trend towards the south and southeast (Claoue-Long and Hoatson 2005; Lawson-Wyatt 2012). The Strangways Event (c. 1730–1700 Ma) attained peak *P–T* conditions of 10 kbar and 850 °C in the southern Aileron Province (Biermeier et al. 2003) but is so far unknown from the Warumpi Province. Protolith ages for sediments in the Warumpi Province span the range 1690–1630Ma (Claoue-Long and Hoatson 2005) and include the time interval of the *Argilke Event* (1680–1660 Ma), a tectnothermal event restricted to the Haasts Bluff Domain that was responsible for the formation of felsic volcanics in the Madderns Yard Metamorphic Complex of the Haasts Bluff Domain (Collins and Shaw 1995; Morrissey et al. 2011; Scrimgeour et al. 2005b). Scrimgeour (2003) interpreted this event to have occurred in a continental crust fragment outboard of the NAC.

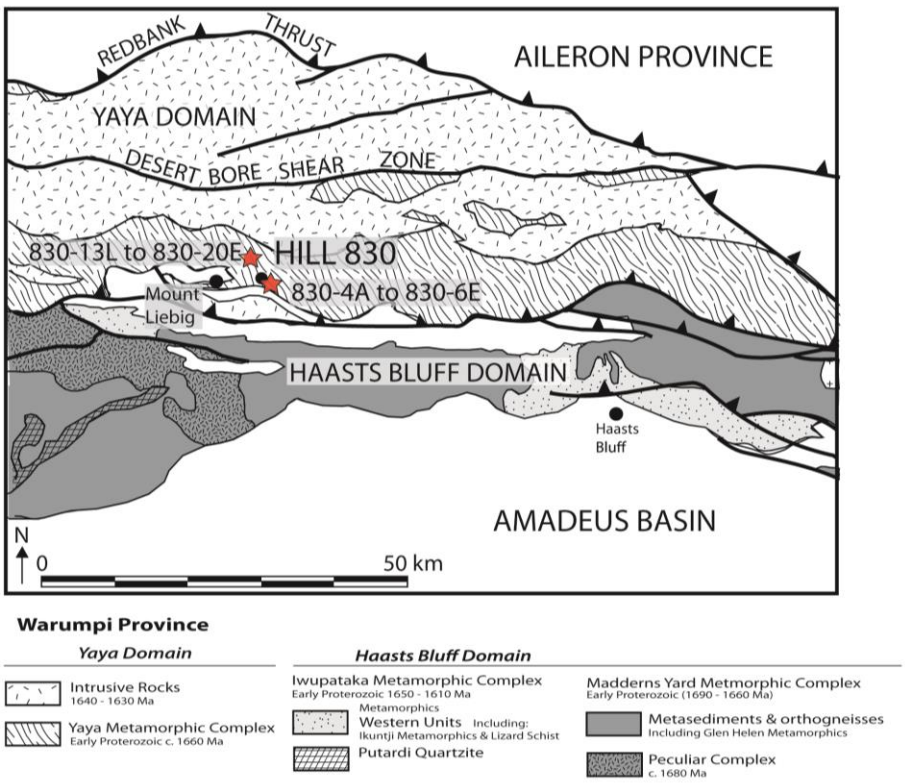

Figure 2: Simplified geological map showing the geological domains of the Warumpi Province, the sample locations and units of significance to this study. Adapted from Wong et al. (2015/in press)

Between 1640–1630 Ma a province-wide tectnothermal event, the Liebig Orogeny, occurred, proposed to reflect the oblique accretion of the Warumpi Province to the Northern Australian Craton (Scrimgeour et al. 2005b). This event reached temperatures greater than 800 °C and pressures of 9–10 kbars (see next subsection), and is characterised by deep burial and exhumation of the Yaya Domain, voluminous magmatism (e.g. Fields 2012) and by the apparent polar wander at the time showing a hairpin bend in the record (Selway et al. 2009; Scrimgeour et al. 2005). The highest grades of metamorphism are those observed at Hill 830 (Close et al. 2003; Scrimgeour et al. 2005b) in the Mt Liebig area (Fig. 2).

The Chewings Orogeny at 1590–1570 Ma was a high-grade deformation metamorphic event experienced across the southern and central Arunta Region, said to represent the most important reworking event experienced by the Warumpi Province and southern Northern Australian Craton (Scrimgeour et al. 2005b) reaching granulite facies metamorphism in the Aileron Province (Claoue-Long and Hoatson 2005). Recent studies (Morrissey et al. 2011; Wong et al. 2015/in press) have shown the extent of deformation by the Chewings Orogeny in the southern Aileron Province and Warumpi Province is more discrete than previously thought, with past structural reworking now shown to represent younger deformation (next subsection).

Following the Chewings Orogeny, Grenvillian-aged (c. 1150–1130 Ma) regional-scale deformation and metamorphism occurred in the Warumpi Province (Morrissey et al. 2011; Wong et al. 2015/in press). This reworking event is recorded in the Warumpi Province and is synchronous with part of the long-lived Musgrave Orogeny (of the Musgrave Inlier exposed ~300 km to the south) (Smithies et al. 2011; Walsh et al. 2015/in press) as part of a larger and widespread Grenvillian-aged tectonic system that also includes the Albany–Fraser Orogen which extends into formerly contiguous Antarctica (Howard et al. 2015/in press ; Morrissey et al. 2011). The metamorphic conditions during this Grenvillian-aged event range across the province. Morrissey et al. (2011) experienced low geothermal gradients of 50°C/km, Fields (2012) recorded 260°C variation across the peak field proving difficult to constrain a peak gradient at 7-8kbar, and Wong et al. (2015/in press) documented the deformation over 110 km in an east–west direction from Alice Springs (east) to the Teapot Granite (west), recording thermal gradients between 125–170 °C $kbar^{-1}$. This (east-west) deformation does not

appear north of the Redbank thrust (Lawson-Wyatt 2012; Wong et al. 2015/in press). In the Yaya Domain this event is characterised by felsic and alkalic magmatism, intrusion of the Teapot Granites at 1136 ± 6 Ma, pegmatites, as well as localised migmatisation (Collins and Shaw 1995; Morrissey et al. 2011; Scrimgeour et al. 2005a; Scrimgeour et al. 2005b). Morrissey et al. (2011) interpreted that the dominant structural trend of the Warumpi Province is Grenvillian-aged, rather than a result of the Chewings Orogeny. At 1080 Ma the Sturt Pass Dolerite Dyke intruded, synchronous with the *Giles Event* in the Musgrave Inlier (Evins et al. 2010; Kirkland et al. 2013; Scrimgeour et al. 2005a; Smithies et al. 2011, Smithies et al. 2015; Wingate et al. 2004).

Exhumation of the Arunta Region from beneath the formerly contiguous Centralian Superbasin occurred during the Alice Springs Orogeny at 450–300Ma (Raimondo et al. 2014). This long-lived intraplate basin inversion event causing substantial reworking and exhumation (Buick et al. 2001; Moeller et al. 2003; Raimondo et al. 2001; Raimondo et al. 2014; Scrimgeour et al. 2005b).

Documented c. 1640Ma Magmatism in the Arunta Region

Throughout the Arunta region, in detail the southern Aileron and Warumpi Provinces, there is parallel c. 1740- 1780Ma and c. 1640Ma magmatism (Claoue-Long and Hoatson 2005; Fields 2012; Young et al. 1995). The presence of these timelines as shown on Table 1, indicate that there was a substantial event acting upon both provinces. The Andrew Young Hill Complex in the southern Aileron Province is characteristic of mafic–ultramafic intrusions aged 1632.9 ± 2.8 Ma (Claoue-Long and Hoatson 2005) and 1635 ± 9 Ma (Young et al. 1995). Further north, Lawson-Wyatt

(2012) found c. 1640Ma magmatism in the Mt Hay region of the Aileron Province. This proposes a magmatic event, following the Inkamulla Event, between the Argilke Event and Chewings Orogeny in the Arunta Region, timely to the Liebig Orogeny in the Warumpi Province. In the Warumpi Province, the Papunya mafic intrusions south of the Redbank shear zone are dated at 1636.5 ±2, 1639.2 ±2, 1634.6 ± 5Ma (Claoue-Long and Hoatson 2005), in addition to c. 1750Ma magmatism found by Fields (2012) in the northern Warumpi. The adjacent gabbro body to Mg-Al rich granulites at Hill 830, is interpreted to have occurred in the same event that emplaced c. 1630- 1640Ma magmatism, suggested to represent extensional cycles migrating south through the Arunta Region (Fields 2012; Claoue-Long and Hoatson 2005).

Study Area

The study area of Hill 830 is located roughly 200 km west of Alice Springs, in the Mount Liebig area of the Warumpi Province (Figs 1 and 2). The Warumpi Province is separated from the Aileron Province by a series of thrusts and shear zones trending east–west, including the Redbank Thrust Zone shown in Fig. 2 (Scrimgeour 2003).

From satellite imagery Hill 830 appears as a large-scale ‘boudin’, bound by strongly foliated east–west trending migmatites and gneisses (Fig. 3). This large-scale boudin comprises gabbro and a smaller outcrop amount of deformed calc-silicate (Fig. 4d) and Mg–Al-rich granulite that for the most part contains little or no fabric (Figs. 3, 4). The gabbro of Hill 830 has mineralogical compositions identical to the northern Papunya intrusions (Scrimgeour et al. 2005b). The Hill 830 gabbro has not been directly dated, however, the Papunya Igneous Complex has a magmatic age of 1635 Ma (see Table 1),

corresponding to the timing of metamorphism at Hill 830 (Claoue-Long and Hoatson 2005). Field relationships show that at the km-scale the gneissic, mylonitic and migmatitic rocks outside the boudin containing gabbro and Mg–Al-rich granulite are characterised by an east–west striking foliation, but that at the boudin the foliation orientation is more variable due to the enveloping rocks dipping under (i.e. structurally underlying) the boudin. Kinematic indicators in the fabric of the enveloping gneisses and mylonites show a top-to-the-north north-east shear sense, contrary to Scrimgeour et al. (2005b).

Background to existing thermobarometry

Pressure–temperature estimates from the unusual Mg–Al-rich granulites at Hill 830 provide one of the two important bases that Scrimgeour et al. (2005b) used to argue to for collisional accretion of the Warumpi Province to the NAC at c. 1640 Ma, during the Liebig Orogeny. The maximum ('peak') *P–T* estimates of 9–10 kbar and >800 °C were based on breakdown of coexisting garnet, orthopyroxene and sillimanite to cordierite and sapphirine (Scrimgeour et al. 2005b). However, the *P–T* estimates are open to interrogation for the following reasons: 1) the *P–T* analysis in Scrimgeour et al. (2005b) used constraints from *P–T* grids (Kelsey et al. 2004; Kelsey et al. 2005) and *P–T* pseudosections borrowed from Kelsey et al. (2005). This is, *P–T* pseudosections were not calculated specifically for the Hill 830 granulites. *P–T* grids are not useful for constraining the *P–T* history of specific rocks because the absolute stability of mineral assemblages shown by *P–T* grids commonly does not correspond the actual stability of a mineral assemblage in a specific rock (Kelsey and Hand 2015); 2) Scrimgeour et al. (2005b) assumed that silicate melt was additionally part of the peak metamorphic

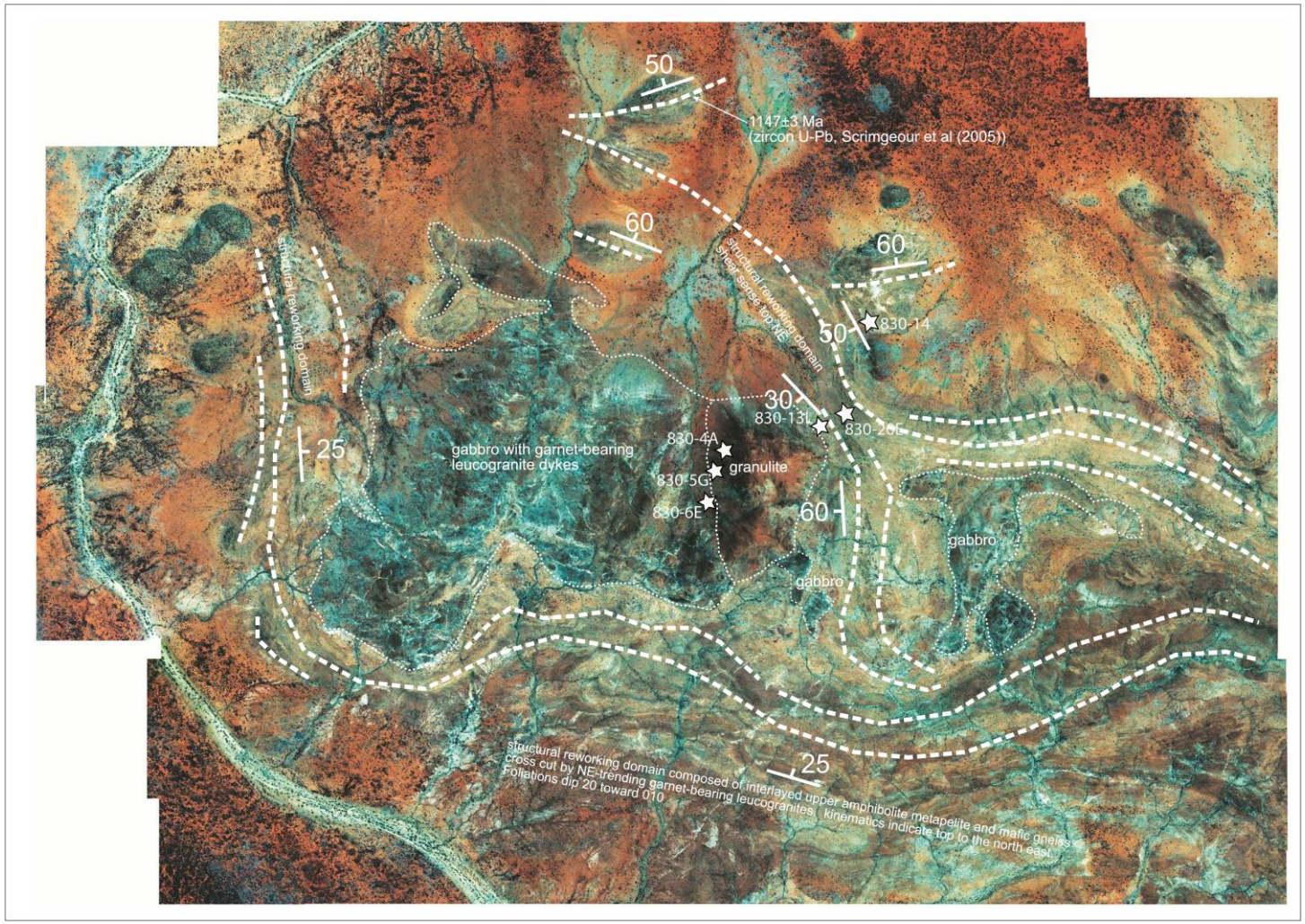

Figure 3: ESRI image of Hill 830, appearing as a dark colour at the centre of the image. Defining fabric of surrounding mylonites, gneisses and migmatites is shown with dashed lines. Small dashed white lines outline the extent of outcrop of gabbro and Mg–Al-rich granulite atop Hill 830. Sample locations are shown by representative stars. Adjacent Gabbro and Hill 830 itself are outlined. Strike and dip directions are shown.

Table 1: Summary of previous studies in the southern Aileron and Warumpi Province in respect to age.

Study	Location	Magmatic Ages (Ma)	Metamorphic Ages (Ma)	PT Conditions	Method	
Claoue-Long and Hoatson 2005 (Northern Warumpi Province, Southern Aileron Province)						
	Andrew Young Hills	1632 ± 2.8			Zircon	
	Papunya gabbro	1636 ± 2.4			Zircon	
	Papunya ultramafic	1639 ± 2.0			Zircon	
	South Papunya gabbro		1634.6 ± 3.4		Zircon	
Biermeier et al. 2003 (Redbank Thrust Zone, Warumpi & Southern Aileron Province)						
310707			1644 ± 13, 1103 ±69		Monazite	
310707 (1)			1771 ± 14		Monazite	
280701			1139± 25, 1767 ± 9		Monazite	
280701 (1)			c. 1630 - 1690		Monazite	
280701 (2 & 3)			c. 1060 – 1191		Monazite	
Fields 2012 (Warumpi & Southern Aileron Province)						
RBN-18	Illyabba Metamorphics		1616 ± 8 , 1819±13	740 – 900℃ 7-8kbar	Monazite	Zircon
RBN-20	Illyabba Metamorphics		1627±7		Zircon	
RBN-43	MYMC		1074 ± 14		Monazite	
RBN-44		1770± 7			Zircon	
RBN-54	MYMC		1096 ± 10, 1767 ± 10		Monazite	Zircon
RBN-57		1747± 6			Zircon	
RBN-61	Illyabba Metamorphics	1739± 7	1625± 7		Monazite	Zircon
RBN-67	Old Hamilton Downs Gneiss	c. 1760	1124±10		Monazite	Zircon
RBN-68	Illyabba Metamorphics	c. 1770	1175, c. 1625		Monazite	Zircon
RBN-71	Old Hamilton Downs Gneiss	c. 1780	1125±10		Monazite	Zircon
AS-2012-1	Illyabba Metamorphics	1633± 9			Zircon	
AS-2012-2	Illyabba Metamorphics	1629± 7	1152 ±34		Zircon	
Lawson-Wyatt 2012 (Mt Hay-Redbank region, Southern Aileron Province)						
RBN-11	Adla Granulite Metapelites (N)		1150 ± 10	780 – 920℃ 5- 10kbar	Monazite	
RBN-12	Adla Granulite Metapelites (N)		1750 ± 6, 1593 ± 20		Monazite	
RBN-26	Adla Granulite Metapelites (C)		1745 ± 6 1642 ± 21		Monazite	
RBN-28	Adla Granulite Metapelites (C)		1741 ± 7		Monazite	
RBN-31	Adla Granulite Metapelites (C)		1750 ± 8		Monazite	
RBN-34	Unnamed Granite	1641 ± 10			Zircon	
RBN-45	Adla Granulite Pegmatite (N)	1627 ± 7	1734 ± 10, 1573 ± 9		Monazite	Zircon
RBN-46	Adla Granulite Pegmatite (N)	1545 ± 7			Monazite	
RBN-47	Adla Granulite Leucosome		1744±9		Monazite	

Table 1 (continued)

Study	Location	Magmatic Ages (Ma)	Metamorphic Ages (Ma)	PT Conditions	Method
Morrissey et al. 2011 (Warumpi Province)					
STC-09-4	Chewings Range Metapelites		1129±11		Monazite
STC-09-8A	Chewings Range Metapelites		1121.9 ± 7.2		Monazite
STC-09-10	Chewings Range Metapelites		1159 ± 24		Monazite
AS-2010-13	Simpsons Gap Metasediments		1149 ± 12		Monazite
AS-09-14	Teppa Hill Sediments		1146±21		Monazite
Blain- 4	Teppa Hill Sediments		1120.1 ±9.9		Monazite
AS-2010-54			1141±22		Sm-Nd
AS-2010-55			1100±22		Sm-Nd
Scrimgeour et al. 2005b (Warumpi Province)					
ML00IR5309	Inyalnga Granite, Hill 830		C: 1880, 625, R: 1638 ± 8		Zircon
ML00DFC132	Alkipipi Metamorphics, Mt Larrie		C: 1750, 1640, R: 1639 ± 20		Zircon
ML00IR5316	Glen Helen Metamorphics		C: 1688 ± 6, R: 1640 ± 12		Zircon
ML00CJE300	Kakalyi Gneiss		C: 1780, 1550, R: 1149 ± 3		Zircon
ML01IR5395	Kakalyi Gneiss (6km W of above)		C: 1644±5, R: 1571±5		Zircon
Smit 2012/in press (Warumpi Province)					
NAC-2011-016		1752± 11			Zircon
NAC-2011-019		1640± 6			Zircon
NAC-2011-033		1627± 26			Zircon
Wong et al. 2015/in press (Southern Aileron Province)					
AS-2010-63D			1090 ± 15		Monazite
AS-2010-67A2			1133 ± 41, 1597 ± 44		Monazite
AS-09-01			1125 ± 11	830℃ 5.7- 6.3kbar	Monazite
AS-2010-65J			1138 ± 17	770- 845℃ 6kbar	Monazite
AS-2010-72D			1129 ± 8		Monazite
RED2011-01			1142 ±10	755- 850℃ 5- 9.5kbar	Monazite
RBN-67			1124 ± 10		Monazite
RBN-71			1122 ±11		Monazite
RBN-54			1096 ± 10		Monazite
830-10G			1646 ± 27, 1230, 1150		Monazite
830-18			1615 ± 13		Monazite
HAM-2011-02			1134 ± 7		Zircon
HAM-2011-08			1626 ± 7, 1139 ± 19		Zircon
AS-2012-1			1633 ± 9		Zircon
AS-2012-2			1629±7, 1152± 34		Zircon
Young et al. 1995 (Andrew Young Hill Complex, Southern Aileron Province)					
G9	Andrew Young Hill Complex	1635±9Ma			Zircon

assemblage. However, field outcrops are for the most part devoid of leucosomes (and K-feldspar), suggesting that melt was not produced in the Mg–Al-rich granulites to any great extent during c. 1640 Ma metamorphism. K-feldspar is only present in the Mg–Al-rich granulites at the margin of the Mg–Al-rich boudin, and may be related to melting of the enveloping migmatites and gneisses, unrelated to the c. 1640 Ma event (see results and discussion sections). Therefore, for the majority of the Mg–Al-rich granulite boudin it is questionable whether silicate melt was part of the peak metamorphic assemblage. If melt was not part of the peak metamorphic assemblage, *P*–*T* conditions can be lower (e.g. Kelsey et al. 2004; Kelsey et al. 2005).

METHODS

Bulk Rock and Mineral Chemistry

WHOLE ROCK GEOCHEMISTRY

Whole-rock geochemical analyses for phase equilibria forward modelling for all samples was undertaken by Wavelength Dispersive X-ray Fluorescence (WD–XRF) spectrometry at the Department of Earth and Environment, Franklin and Marshall College, Lancaster PA, USA. Major elements were analysed on fused disks prepared using a lithium tetraborate flux.

ELECTRON MICROPROBE

Mineral composition (‘spot’) analysis and elemental mapping of parts of thin sections were obtained using the Cameca SXfive Electron Microprobe at Adelaide Microscopy (The University of Adelaide). Analysis of samples were undertaken through both X-Ray Map and Spot Analysis. X-Rap Map analyses was performed for elements Si, Al, F, Fe,

Na, Ca, K, P, Mn, Mg, Ce, Ti and Zr under beam conditions of 100nA and 20kV. For elemental analysis these settings were 20nA and 15kV.

Geochronology

U–PB MONAZITE LA–ICPMS GEOCHRONOLOGY

Analytical techniques for U–Pb isotopic dating of monazite are similar to those of Payne et al. (2008). Monazites were imaged on a Phillips XL-30 Field Emission Scanning Electron Microscope (FESEM) to determine their location in thin section, define any associated spatial distributions and any internal zoning of monazite grains. U–Pb isotopic analyses were obtained using a New Wave 213nm Nd–YAG laser in a He ablation atmosphere, coupled to an Agilent 7500cs/7500s ICP–MS at Adelaide Microscopy (The University of Adelaide). Ablation of monazites was performed with a frequency of 5Hz and a spot size of 15 µm, with a total acquisition time of 80 s, including 30 s of background measurement, 10 s of the laser firing with the shutter closed to allow for beam stabilization, and 40 s of sample ablation. Isotopes measured were ^{204}Pb, ^{206}Pb, ^{207}Pb and ^{238}U for dwell times of 10, 15, 30 and 15ms respectively.

Monazite data was documented using Glitter software (Griffin et al. 2004). Fractionation of elements and mass bias were corrected for using known standard MAdel (TIMS normalization data: ^{206}Pb/^{207}Pb= 490.7Ma, ^{206}Pb/^{238}U= 514.8Ma and ^{207}Pb/^{235}U=510.4Ma: Payne et al. (2008) with an overestimated uncertainty of 1% attached to each normalization age. Data accuracy was monitored and corrected by repeated analysis of known, in-house standard, 222. Standard MAdel and 222 peaks, along with unknown signals were examined to ensure there were no anomalous signals

in respect to Pb loss or gain, selecting the best signal portions for final date and error analysis. In this study MAdel as a primary standard had consistent weighted mean ages of $^{206}Pb/^{207}Pb$= 502.6 ± 8.4Ma, $^{206}Pb/^{238}U$= 515.4 ± 1.9Ma and $^{207}Pb/^{235}U$= 513.1 ± 1.9Ma (n=66), and unknown internal standard 222 yielded weighted mean ages of $^{206}Pb/^{207}Pb$= 457 ± 11Ma, $^{206}Pb/^{238}U$= 455.1 ± 3.7Ma and $^{207}Pb/^{235}U$=455.1 ± 3.5Ma (n=45). Standard analyses results are attached in Appendix B. Instrument drift was also corrected for with the application of a linear correction and by standard bracketing every five analyses for monazite. Weighted average ages collected throught the couse of this study for in-house monazite standard 222 were $^{207}Pb/^{206}Pb$ = 453.6±6.0 Ma (n=78, MSWD=0.41), $^{206}Pb/^{238}U$ = 449.3±1.5 Ma (n=69, MSWD=1.07), and $^{207}Pb/^{235}U$ = 450.6±1.6 Ma (n=72, MSWD=1.4) and MADel were $^{207}Pb/^{206}Pb$ = 492.5±5.7 Ma (n=90, MSWD=0.35), $^{206}Pb/^{238}U$ = 517.0±1.6 Ma (n=87, MSWD=1.14), and $^{207}Pb/^{235}U$ = 511.8±1.4 Ma (n=84, MSWD=0.92).

Phase forward equilibria modelling

Phase equilibria calculations were performed using the software programs THERMOCALC and Perple_X (Powell and Holland 1988; Holland and Powell 2011; Connolly 2005; Connolly and Petrini 2002) in the chemical system MnO–NaO–CaO–K2O–FeO–MgO–Al2O3–SiO2–H2O–TiO2–O, where ‘O’ is Fe2O3, using the special version of the internally-consistent thermodynamic dataset ‘ds5’ that allows calculations with sapphirine and osumilite (filename tc-ds55s.txt; Holland and Powell 1998; Kelsey et al. 2004). The activity–composition relationships used were: silicate melt, garnet and biotite (White et al. 2007); orthopyroxene and magnetite (White et al. 2002); cordierite

(Holland and Powell 1998); ilmenite (White et al. 2000); plagioclase and K-feldspar (Holland and Powell 2003); and sapphirine (Taylor-Jones and Powell 2010).

Calculations in THERMOCALC are based on the user specifying the stable assemblage and calculating the diagram line by line, point by point, where lines (field boundaries) represent the zero abundance of a phase and points represent the zero abundance of two phases. The initial stable assemblage is determined by performing a Gibbs energy minimisation calculation at a set pressure–temperature (*P*–*T*) condition. The diagram is built up and around from that initial assemblage and involves many trial and error calculations in order to determine which phases appear or disappear as a function of pressure, temperature and/or composition. In addition, the so-called 'starting guesses' (values for compositional variables for phases with which THERMOCALC commences its iterative least-squares calculation for a line or point) require regular updating as the pseudosection is calculated in different parts of *P*–*T*–*X* space (*X* is composition). Therefore, a single diagram commonly comprises >150–200 total line and point calculations, and the user is actively (intellectually), rather than passively, involved in the calculations at every step along the way (this amounts to a considerable amount—up to several weeks—per diagram). The most uncertain compositional variables are Fe_2O_3 and H_2O, commonly requiring that these be constrained with *T*–*M* type diagrams (where *M* refers to amount of an oxide component) prior to the calculation of the pressure–temperature (*P*–*T*) pseudosection. The choice of pressure at which to calculate the *T*–*M* diagrams is based on broadly estimating the pressure at which the petrographically-determined peak metamorphic assemblage is stable. Calculations in Perple_X are based on Gibbs energy minimisation over a user-specified gridded *P*–*T* or *T*–*X* range. The

calculation of pseudosections in Perple_X is automated such that the user only need specify the rock ('bulk') composition, the list of solid-solution phases to be used by the calculation process, the name of the thermodynamic dataset and the *P–T* range. Some pseudosections have been calculated in Perple_X for the sake of time constraints, but it is by using THERMOCALC that the skill set of learning phase equilibria is developed.

RESULTS

Metamorphic Petrology

OUTCROP FEATURES, SAMPLE SELECTION AND PETROGRAPHY

Samples used for this study are exceedingly fresh and were chosen on the basis of mineralogy and mineral reaction microstructures, as well as field structural location (e.g. Mg–Al-rich granulite vs enveloping gneiss/migmatite). This domain, outside and structurally below Hill 830 preserves a dominant east-west trending fabric, with abundant leucosomes and foliation that dips vertically between 350 and 10° north. Sample 830-20E is from a smaller scale boudin within the enclosing migmatised zone surrounding the undeformed rocks at Hill 830.

Table 2: Summary of location, lithologies and analyses of each sample used in this study

Sample No.	Easting	Southing	Lithology	Type of Analysis	Relative Location
830-4A	0761488	7425700	Mg–Al-rich Gt-opx-sill-cd Granofels	Petrography + U-Pb Monazite	Hill 830
830-5G	0761433	7425695	Mg–Al-rich Gt-opx-sill-cd Granofels	Petrography, U-Pb Monazite + Mineral Chemistry	Hill 830
830-6E	0761284	7425663	Mg–Al-rich Gt-opx-sill-cd Granofels	Petrography, U-Pb Monazite, Mineral Chemistry + Mineral Equilibria Modelling	Hill 830
830-13L	0761900	7425900	Gt-cd-sill-bi-st Gneiss	Petrography + U-Pb Monazite	Enclosing Migmatites
830-14	0762226	7426506	Gt-cd-sill-bi Gneiss	Petrography, U-Pb Monazite, Mineral Chemistry + Mineral Equilibria Modelling	Enclosing Migmatites
830-20E	0762108	7425922	Gt-cd-sill-bi Gneiss	Petrography + U-Pb Monazite	Enclosing Migmatites

Hill 830 Mg–Al-rich granulites

In thin section these samples (830-4A, 5G, 6E) are composed predominately of garnet, sillimanite, orthopyroxene, cordierite, magnetite, ilmenite, quartz and biotite. In all studied Mg–Al-rich samples there is also a high concentration of highly radiogenic (based on size of radiation damage haloes in cordierite) monazite (Fig. 5c). The samples are rich in reaction microstructures and mineralogy, making them particularly useful for thermobarometry. Coarse-grained (2-4 mm) garnet and orthopyroxene poikiloblasts are abundant and define a moderate to strong fabric in thin section. Garnet and orthopyroxene mostly remain in direct contact with each other. Garnet contains inclusions of biotite, ilmenite, magnetite and sillimanite. Orthopyroxene contains inclusions of sillimanite, biotite, magnetite and minimal k-feldspar (Fig. 9) and exclusively in Sample 5G, rutile. Orthopyroxene is in direct contact with large quartz throughout e.g. Fig. 8. Coarse-grained (0.5-1 mm) sillimanite is restricted to garnet-rich and coarse-orthopyroxene-absent regions of the rock. Cordierite is abundant in the sample and defines much of the matrix in garnet- and coarse-orthopyroxene-bearing regions. Cordierite occurs as ‘patches’ that are particularly recognisable in coarse-orthopyroxene-rich parts of the sample on the basis of fine-grained sillimanite inclusions within them (Figs. 5f, 9, 10). Sillimanite is oriented within a given patch of cordierite but is not oriented when multiple/many cordierite patches are viewed (Figs. 5b, 5f). Cordierite also contains small inclusions of magnetite, ilmenite, quartz, fine-grained orthopyroxene and rarely biotite (Figs. 9, 10). In rare situations the cordierite ‘patches’ have a distinct rectangular shape and at the contact with quartz are partially laced with fine-grained orthopyroxene (Figs. 5f, 8, 10). In garnet-rich regions, cordierite is typically characterised by its association/contact with fine-grained orthopyroxene, biotite, magnetite and ilmenite. Quartz has a low abundance in the sample and occurs in contact with cordierite, coarse and fine-grained orthopyroxene and garnet (Figs. 5a, 5b, 5c, 5f). Biotite occurs as a mix of coarse and fine-grains in direct contact

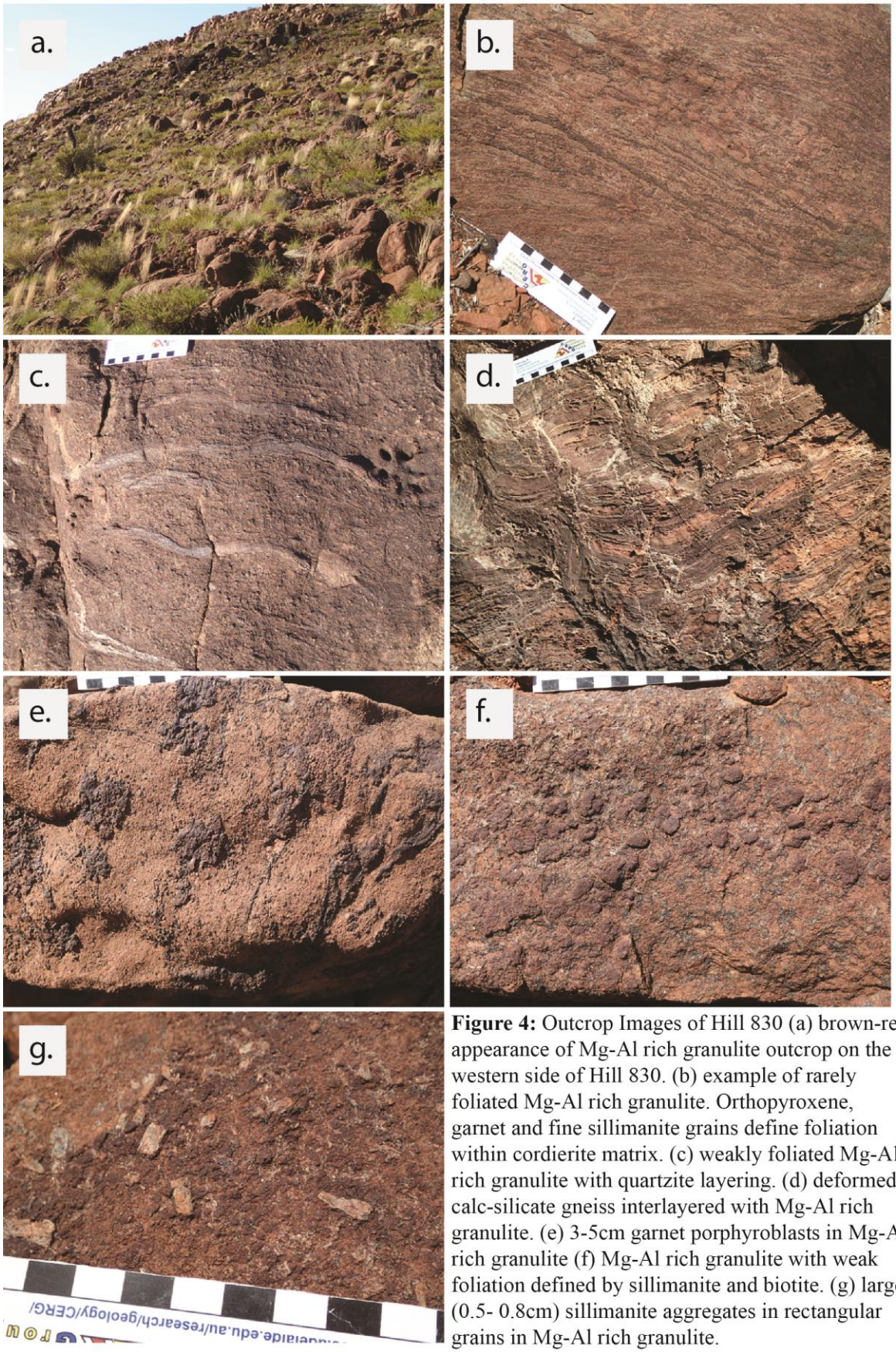

Figure 4: Outcrop Images of Hill 830 (a) brown-red appearance of Mg-Al rich granulite outcrop on the western side of Hill 830. (b) example of rarely foliated Mg-Al rich granulite. Orthopyroxene, garnet and fine sillimanite grains define foliation within cordierite matrix. (c) weakly foliated Mg-Al rich granulite with quartzite layering. (d) deformed calc-silicate gneiss interlayered with Mg-Al rich granulite. (e) 3-5cm garnet porphyroblasts in Mg-Al rich granulite (f) Mg-Al rich granulite with weak foliation defined by sillimanite and biotite. (g) large (0.5- 0.8cm) sillimanite aggregates in rectangular grains in Mg-Al rich granulite.

with orthopyroxene, quartz and cordierite (Figs. 5a, 5c). There is a very small (< 1%) amount of plagioclase in the sample and it occurs in the matrix e.g. Fig. 9. Sapphirine occurs only in Sample 830-4A as rare anhedral grains (1 mm size) in the cordierite-rich matrix and does not occur in contact with coarse garnet, orthopyroxene or sillimanite.

There is a distinct fabric that appears mostly in garnet layering within the samples; however fine-grained orthopyroxene and sillimanite are orientated differently to this main garnet fabric. These differences in fabric define two domains within the thin section. In the OPX-Sill domain there are repeated rectangular shapes, consisting of biotite, sillimanite and extensive oxide and monazite rich cordierite (Figs. 5e, 5f). Here, there is both coarse and fine-grained, sillimanite and orthopyroxene grains, with the smaller OPX grains growing around the outside of rectangular regions of which the smaller sillimanite needles are orientated randomly within. These patches of cordierite containing oriented, fine-grained sillimanite are interpreted to represent former andalusite that was pseudomorphed by sillimanite and then partially replaced by a cordierite-bearing assemblage. In garnet domains the grains appear 'snowflake' like and do not hold any other these pseudomorphed rectangular regions.

For the Mg-Al rich granulites the peak assemblage is interpreted to be garnet + orthopyroxene + sillimanite + quartz + biotite + ilmenite + magnetite and the post-peak assemblage is interpreted to involve cordierite, magnetite, ilmenite, biotite and fine-grained orthopyroxene. Fine-grained sillimanite is interpreted to be relict, partially replaced by cordierite. Exceptions to the post-peak assemblage is for 830-4A with the addition of sapphirine.

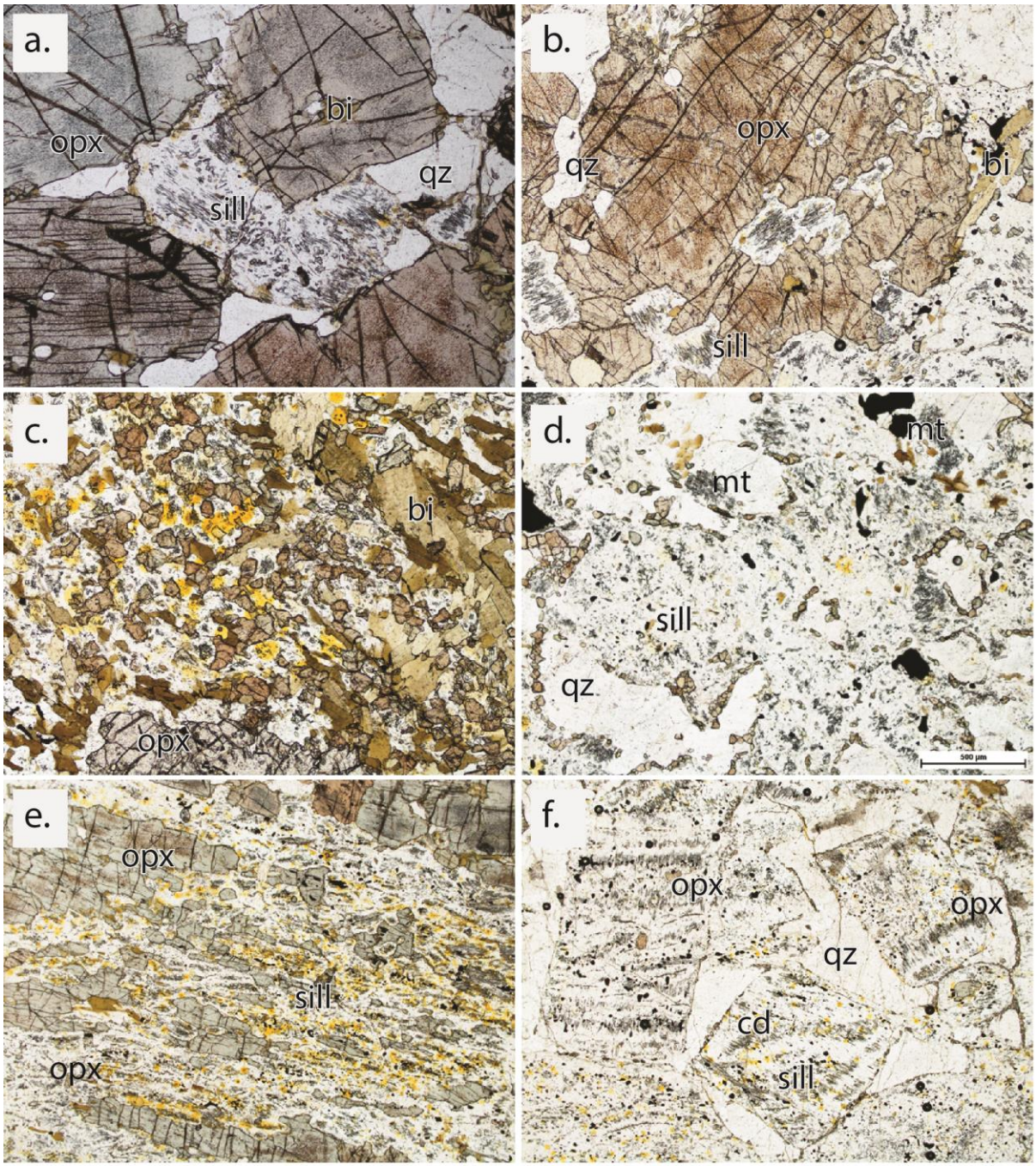

Figure 5: Thin Section Images; (a) is from sample 830-4a, (b), (c) and (d) are from sample 830-5g, and (e) and (f) are from sample 830-6e. (a) coarse orthopyroxene (with exsolution of rutile) in direct contact with quartz surrounds a cordierite-bearing region that contains fine-grained, partly orientated inclusions of sillimanite and magnetite. Fine-grained orthopyroxene partly defins the outside of the cordierite-bearing region. (b) mineral within orthopyroxene grain, fine-grained internal sillimanite needles do not come into contact with orthopyroxene. (c) cordierite-bearing matrix with fine-grained orthopyroxene and biotite. Cordierite contains abundant inclusions of moazite, as shown by the bright yellow radiation haloes. (d) fine-grained sillimanite-bearing domains that are partially ringed by a 'necklace' or corona of fine-grained orthopyroxene. (e) elongate, coarse orthopyroxene separted from sillimanite by abundant cordierite. Sillimanite is locally orientated at the scale of an individual 'patch' of cordierite by is not oriented at a slightly larger scale. (f) rectangular and square domains containing a cordierite dominated matrix, with oriented sillimanite and bordered by a 'necklace' of fine-grained orthopyroxene.

Enveloping gneissic and mylonitic domain

The region outside the boudin (Fig. 3) is composed of deformed (gneissic, mylonitic) and migmatised garnet-bearing gneisses (Fig. 6). The transition from the boudin into the enveloping gneisses is sharp, with no interlayering of the two packages visible. The gneisses show an overall east–west trending foliation with a top-to-north shear sense (Figs. 6c, 6d).

830-13L

This sample contains garnet, cordierite, biotite, spinel and sillimanite. There is no obvious fabric in the sample. Garnet and biotite, and garnet and magnetite/ilmenite are consistently separated by cordierite and quartz. Throughout the sample cordierite includes strauolite, and additionally in these domains fine-grained spinel is either located in direct contact with, or in very close proximity of staurolite grains. The peak assemblage here is biotite-garnet-sillimanite-strauolite-magnetite-ilmenite-quartz and melt, and post-peak biotite-garnet-cordierite-strauolite-magnetite-ilmenite-quartz-sillimanite and spinel.

830-14

This sample contains garnet, sillimanite, biotite, magnetite, ilmenite, cordierite and abundant quartz. There is a prominent, almost mylonitic fabric defined by sillimanite and biotite. Garnet grains are rounded but embayed and are commonly surrounded by cordierite. Cordierite only occurs surrounding and in direct contact with garnet (Fig. 12). Large grains of magnetite appear heavily broken down by quartz. The peak assemblage is interpreted to be biotite-garnet-magnetite-ilmenite-sillimanite-quartz and melt, and post- peak assemblage biotite-garnet-magnetite-ilmenite-sillimanite-quartz and sillimanite.

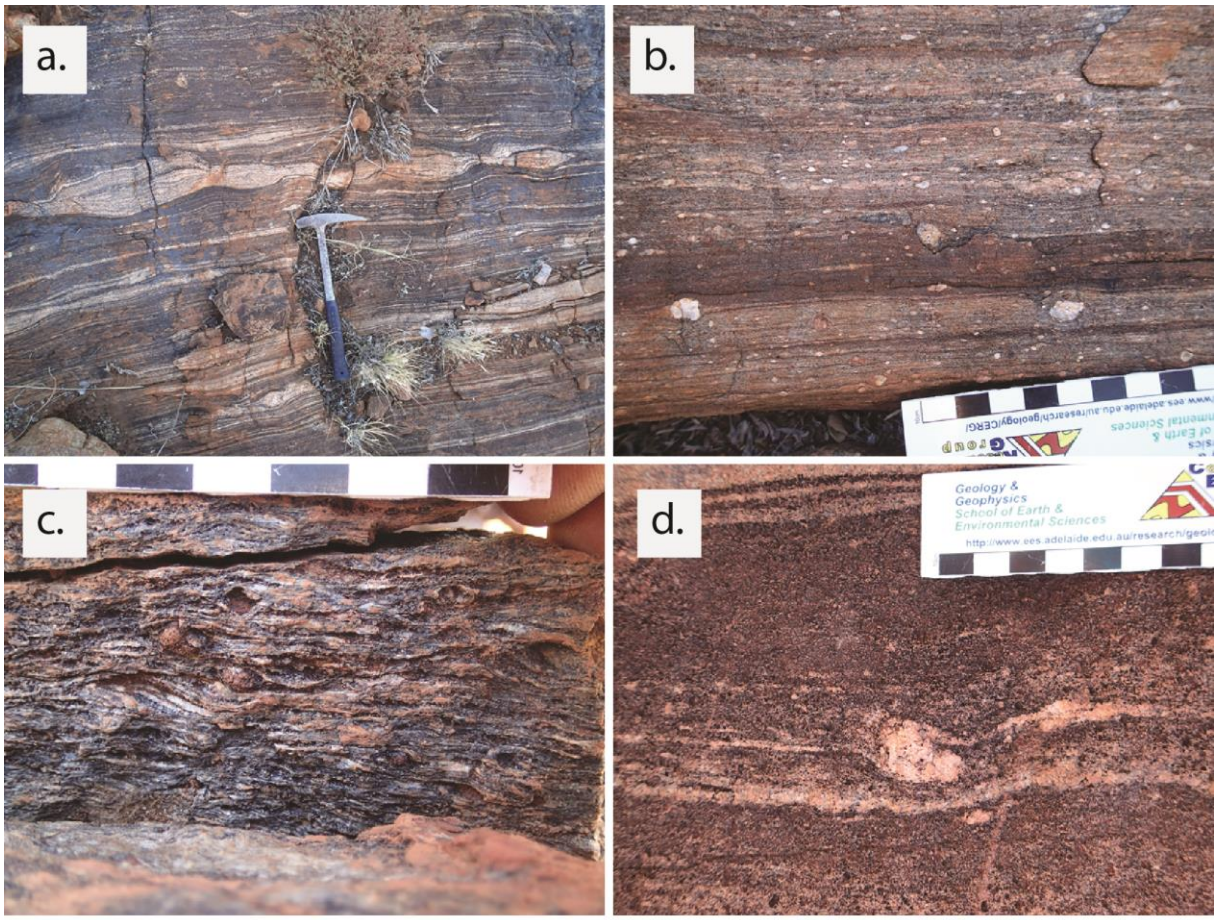

Figure 6: Outcrop Images from migmatities that surround Hill 830 (a) strongly layered migmatic gneiss on the northern side of Hill 830. (b) mylonitic felsic gneiss from the south-east trending fabric domain north-east of Hill 830. (c) S-C style fabric in gt-cd-sill-bi gneiss from south of Hill 830, showing top north shear sense (toward the left). (d) delta-style k-feldspar porphyroclast in the south-east trending reworking fabric domain showing top to the north north-east shear sense (left).

Small Scale Enclave

This location (Fig. 3) is a mixture of the Hill 830 outcrop and surrounding gneiss. There is a clear domain of cordierite and sillimanite grains, although the surrounding migmatised foliations merge with the internal outcrop indicating a simultaneous event.

830-20E

This sample is strongly foliated with the main fabric defined by biotite, which orients around larger K-feldspar, opx, quartz and smaller garnet grains (Fig. 7d). These large K-feldspar and quartz grains define much of the sample. In this sample the fabric is defined by aligned biotite. Large orthopyroxene grains cross cut fabric with sharp grain boundaries, whereas smaller opx grains are angled with the fabric (Fig. 7c). Magnetite, ilmenite and monazite grains are present in this fabric. The peak assembalge is interpreted to be garnet-quartz-biotite-magnetite-ilmenite-orthopyroxene-quartz and melt, and post-peak assemablage garnet-quartz-magnetite-ilmenite-orthopyroxene-biotite and k-feldspar.

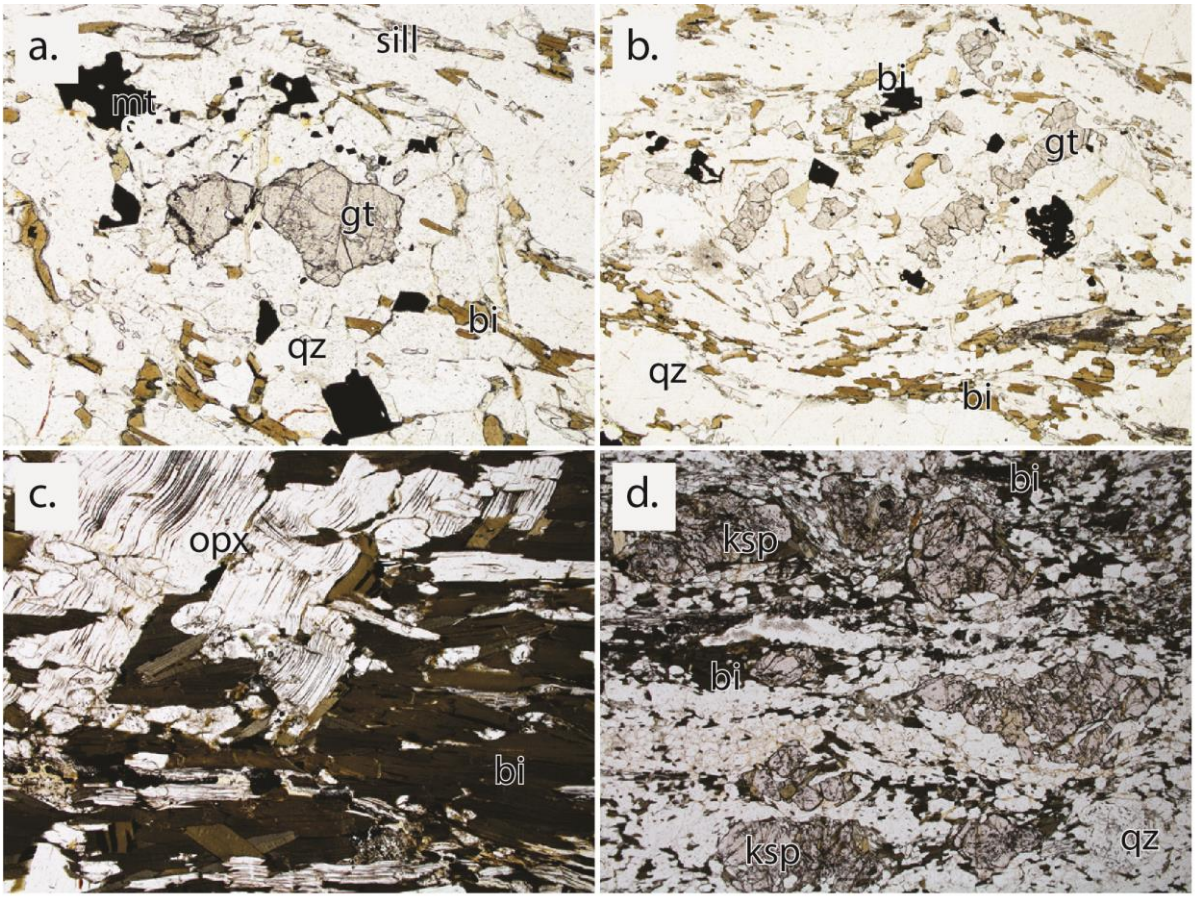

Figure 7: Thin Section Images; (a) and (b) are of sample 830-14 and (c) and (d) of sample 830-20e. (a) unorientated garnet grain surrounded by quartz. The fabric is defined by biotite and sillimanite. (b) biotite and sillimanite orientated in a quartz matrix. (c) orthopyroxene grains cross-cutting dominant biotite fabric. (d) large potassium feldspar grains centred in a strongly orientated fabric.

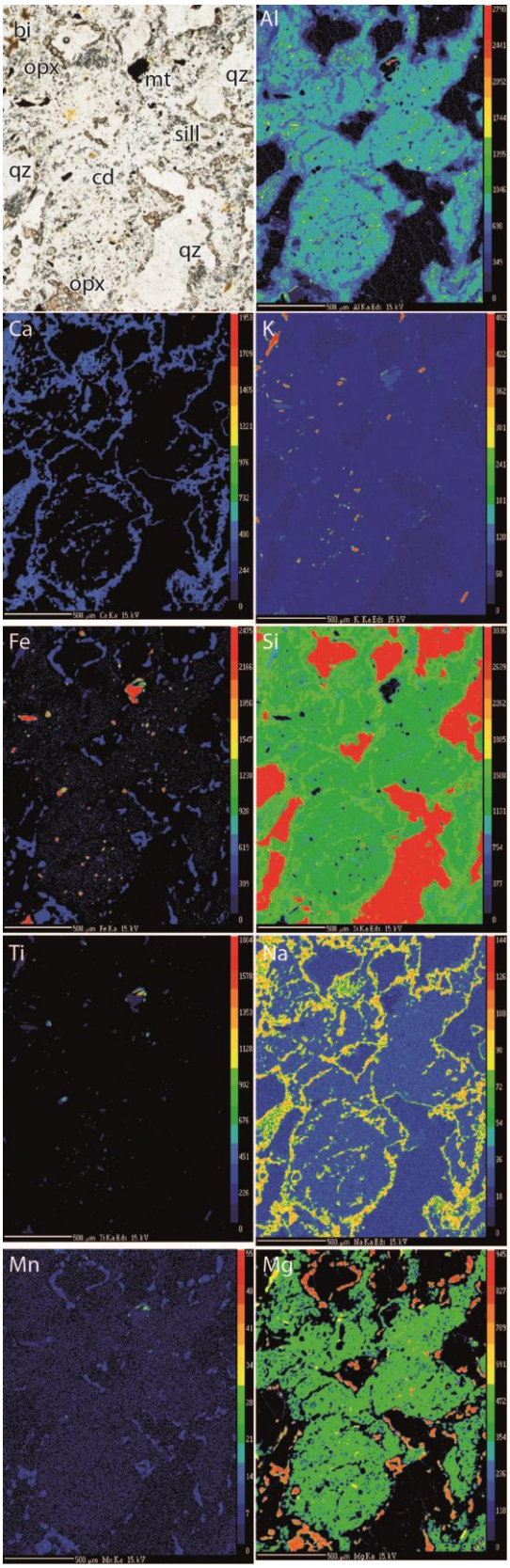

Figure 8: Microprobe elemental maps for Sample 830-5g (Map B) of Al, Ca, K, Fe, Si, Ti, Na, Mn and Mg for an area demonstrated in the top left corner with associated minerals labelled.

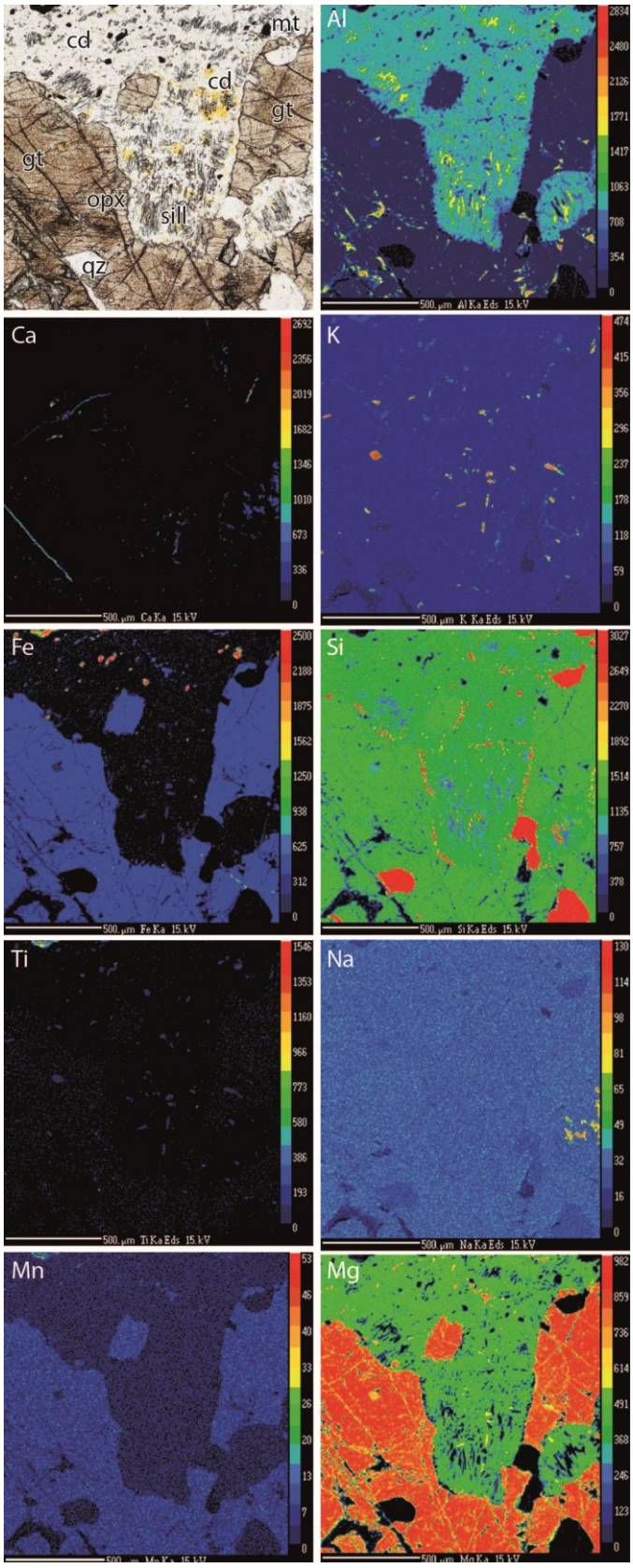

Figure 9: Microprobe elemental maps for Sample 830-5g (Map D) of Al, Ca, K, Fe, Si, Ti, Na, Mn and Mg for an area demonstrated in the top left corner with associated minerals labelled.

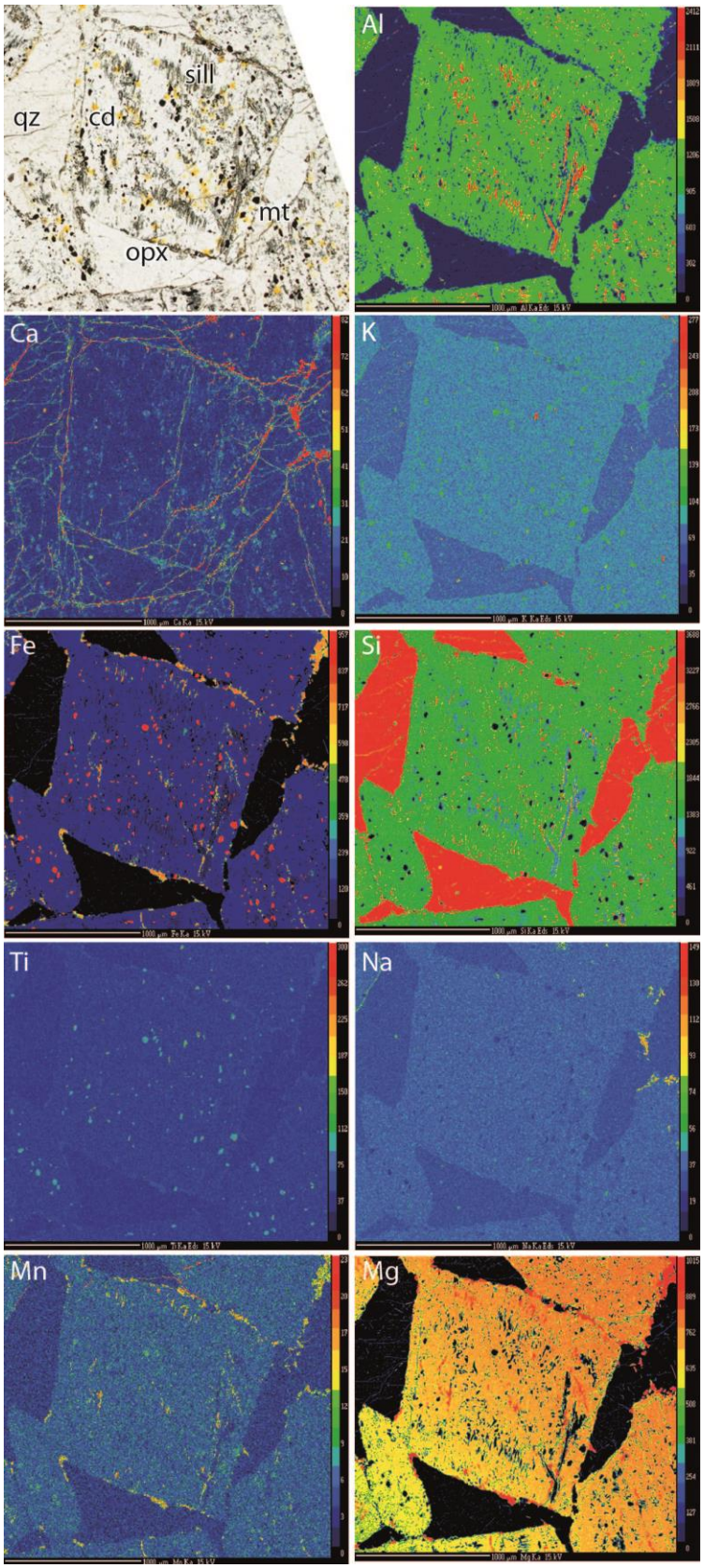

Figure 10: Microprobe elemental maps for Sample 830-6e (Map A) of Al, Ca, K, Fe, Si, Ti, Na, Mn and Mg for an area demonstrated in the top left corner with associated minerals labelled.

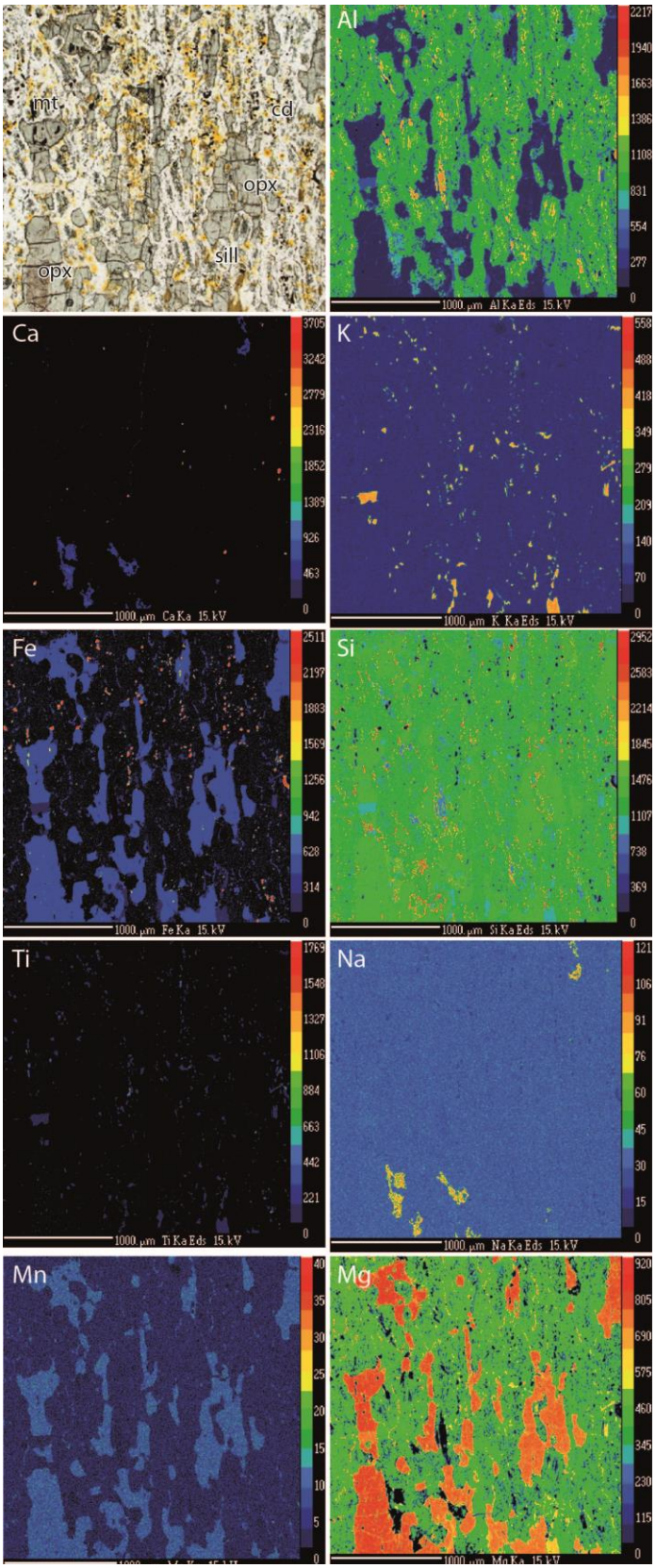

Figure 11: Microprobe elemental maps for Sample 830-6e (Map D) of Al, Ca, K, Fe, Si, Ti, Na, Mn and Mg for an area demonstrated in the top left corner with associated minerals labelled.

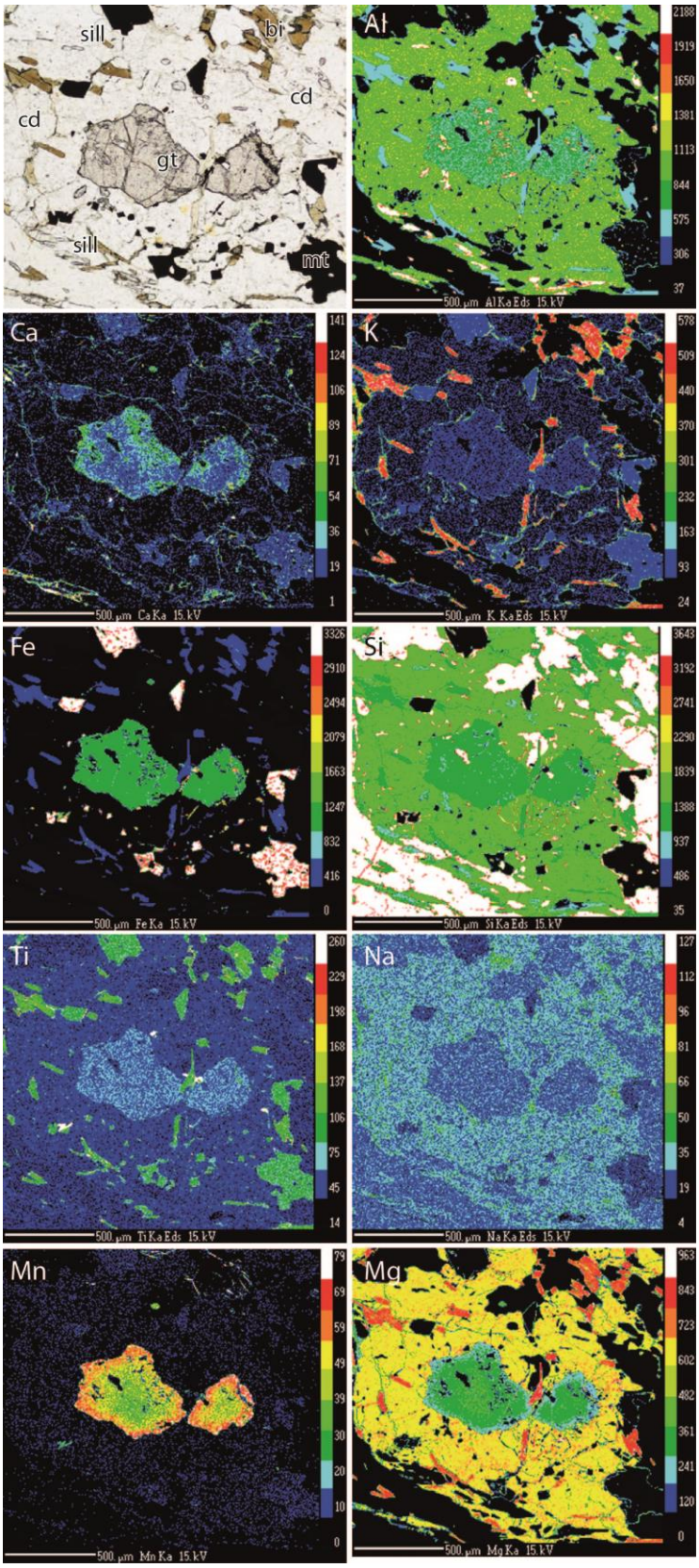

Figure 12: Microprobe elemental maps for Sample 830-14 (Map A) of Al, Ca, K, Fe, Si, Ti, Na, Mn and Mg for an area demonstrated in the top left corner with associated minerals labelled.

Geochronology

U–PB MONAZITE GEOCHRONOLOGY

In this study *in situ* monazite grains were analysed from six samples: 830-4A, 830-5G, 830-6E, 830-13L, 830-14 and 830-20E. All analysed grains were 30–100µm in diameter, and rounded in shape. No zoning was noted for any monazite grains analysed in this study by backscattered electron imaging. For samples 830-4A, 830-5G and 830-6E monazite grains were particularly abundant in cordierite-bearing domains. Overall there was no consistency to the microstructural/mineralogical location of monazite grains and as such, analyses were taken from monazites in different microstructural/mineralogical contexts. All monazite U–Pb age data from this study are presented in Appendix C.

Sample 830-4A

Twenty analyses were taken from 15 grains. The analyses were plotted on a Concordia plot (Fig. 10a). $^{207}Pb/^{206}Pb$ weighted average age of 1637±27Ma (n=8, MSWD= 0.1022) was found in addition to a younger concordia population range of 1538- 1622Ma (n=12).

Sample 830-5G

Twenty analyses were done on 10 monazite grains. The results were plotted on a Concordia plot (Fig. 10b) with an intercept age of 1634 ± 15Ma and $^{207}Pb/^{206}Pb$ weighted average of 1634 ± 12Ma (n=20, MSWD= 0.48). An outlier of 1567 ± 21.4Ma was excluded from weighted average calculations.

Sample 830-6E

Twenty analyses were taken from 15 monazite grains. The analyses were plotted on a Concordia plot (Fig. 10c). An intercept age of 1640 ± 13 Ma was found with a $^{207}Pb/^{206}Pb$ weighted average age of 1640 ± 27 Ma (n=11, MSWD= 1.2).

Sample 830-13L

Eighteen analyses were performed on 15 grains. A Concordia plot was calculated for these analyses yielding a $^{207}Pb/^{206}Pb$ weighted average age of 1131 ± 15 Ma (n=18, MSWD=0.78) and a $^{206}Pb/^{238}U$ weighted average age of 1155 ± 12 Ma (n=18, MSWD= 1.2), shown on Fig. 10d. Due to complications associated with dating in the c. 1000-1200 Ma age bracket both ages are supplied and are notably similar in result.

Sample 830-14

Thirteen analyses were taken from 12 grains in this sample. The analyses were plotted on a Concordia plot (Fig. 10f) with two populations recorded. The younger population has a $^{207}Pb/^{206}Pb$ Concordia age range from 1094- 1208Ma (n=6). The second population recorded a $^{207}Pb/^{206}Pb$ an age range from 1541- 1613Ma (n=3). There is an older $^{207}Pb/^{206}Pb$ weighted average age at 1634 ± 24Ma (n= 3, MSWD= 0.021).

Sample 830-20E

Twenty-two analyses were done on 17 grains. The analyses were plotted on a Concordia plot (Fig. 10e) yielding a $^{207}Pb/^{206}Pb$ age range of 1084- 1205Ma (n=6), and a secondary spread of data from 1532Ma- 1621Ma (n=3).

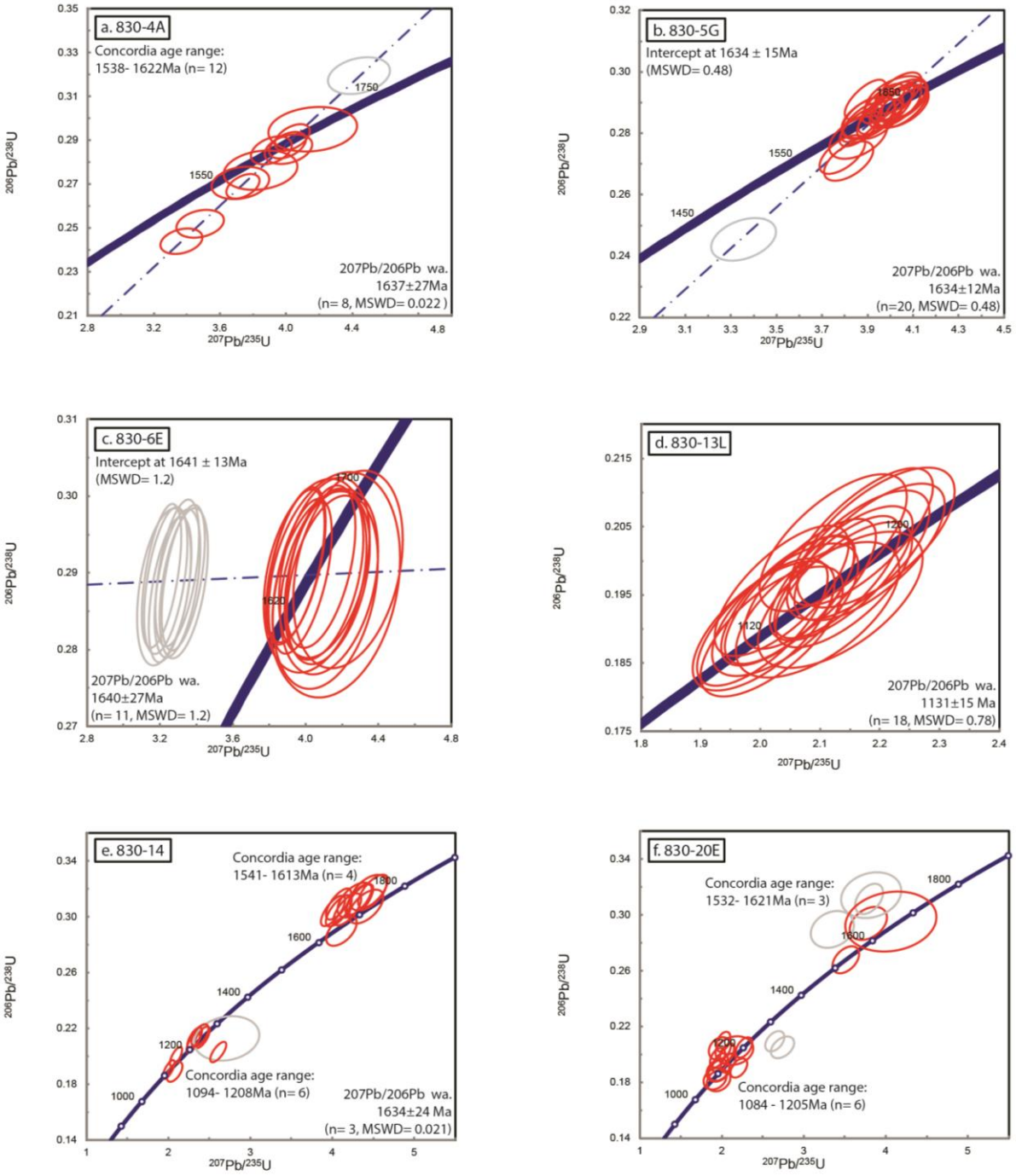

Figure 13: In *situ* LA-ICPMS monazite U-Pb geochronology. All ages shown are $^{207}Pb/^{206}Pb$ ages. (a) 830-4A: Concordia plot with weighted average age and concordia age range given. (b) 830-5G: Concordia plot with weighted average and intercept ages given. (c) 830-6e: Concordia plot with weighted average and intercept ages given. (d) 830-13L: Concordia plot with weighted average age given. (e) Concordia plot with two concordia age ranges and a weighted average age given. (f) Concordia plot with age population distributions.

Pressure-temperature conditions

T–M_O, *T*–M_{H2O} and *P*–*T* pseudosections were calculated for Mg–Al-rich granulite sample 830-6E and enveloping migmatitic gneiss sample 830-14 in order to constrain, respectively, the oxidation state, water content and P–T conditions of the peak and retrograde assemblages of the two samples. In each *T*–M_O section the oxidation state along the *M* axis varies from 0% Fe_2O_3, 100% FeO at *M* = 0 to 66% Fe_2O_3, 34% FeO at *M* = 1. In each *T*–M_{H2O} section the amount of water varies from 0.01 mole% at *M* = 0 to the analysed LOI amount (converted to mole%) at *M* = 1. The fixed pressure for the *T*–M_O and *T*–M_{H2O} sections was chosen to be 9.5 kbar for sample 830-6E and 5.5 kbar for sample 830-14 on the basis of the interpreted peak silicate mineral assemblage (e.g. White et al. 2007).

Table 3: Chemistry of minerals from electron microprobe analysis.

		830-5G	830-6E	830-14
Garnet core				
X_{alm}	Range	0.47-0.53	0.42-0.53	0.68-0.71
X_{py}	Range	0.31-0.51	0.39-0.53	0.24-0.29
X_{grs}	Range	0.015-0.035	0.043-0.059	0.002-0.007
X_{spss}	Range	0.009-0.013	0.016-0.023	0.024-0.035
Garnet rim				
X_{alm}	Range	-	-	0.704-0.726
X_{py}	Range	-	-	0.212-0.254
X_{grs}	Range	-	-	0.002-0.005
X_{spss}	Range	-	-	0.037-0.039
Orthopyroxene				
Ca (y(opx))		0.048-0.096	0.068-0.122	-
X_{Fe}		0.269-0.296	0.255-0.306	-
Biotite				
X_{Fe}		0.181-0.208	0.154-0.194	0.346
Al_2O_3 (wt%)		15.48-18.06	12.37-15.61	18.14
MnO (wt%)		0-0.01	0-0.02	0
TiO_2 (wt%)		2.19-3.53	1.82-2.71	2.42
Cordierite				
X_{Fe}		0.098-0.148	0.097-0.133	0.19-0.47
Magnetite				
TiO_2 (wt%)		20.52	0	0.16
Al_2O_3 (wt%)		0.14	1.08	0.25

The T–M_O diagram for 830-6E in Fig. 14a shows that the stability of magnetite is limited to higher amounts of ferric iron. The peak assemblage field occurs from approximately M_O = 0.2 to 0.75, and from 785 °C to 925 °C. The composition approximately midway across the peak assemblage field (corresponding to M_O = 0.4) was used for the next pseudosection, the T–M_{H2O} diagram, Fig. 14b. In the T–M_{H2O} diagram (Fig. 14b) the peak assemblage occurs towards the low H_2O part of the diagram, as expected. Due to there being small amounts of Ca and Na in the bulk composition, plagioclase (and K-feldspar) are stabilised in the absence of silicate melt. The composition approximately midway across the peak assemblage field (corresponding to M_{H2O} = 0.35) was used for the calculation of the P–T pseudosection.

The P–T pseudosection for sample 830-6E, Fig. 15, shows the peak assemblage field to occur over the P–T range of 8–11 kbar, 700–900 °C. Assemblage fields containing cordierite typically occur at lower pressure (and/or higher temperature) than the peak assemblage field. The peak assemblage field is bound at higher temperatures by the appearance of silicate melt, at lower temperatures by kyanite, rather than sillimanite, stability, and to higher pressures by the disappearance of sillimanite and (minute abundance) plagioclase. Across the peak assemblage field the content of aluminium in orthopyroxene further constrains the peak location when compared to values retrieved through electron microprobe analysis (Table 3). The decompressional path of peak to post-peak assemblages is represented by a white arrow (Fig. 15), adding magnetite and cordierite to the post-peak assemblage through P-T space.

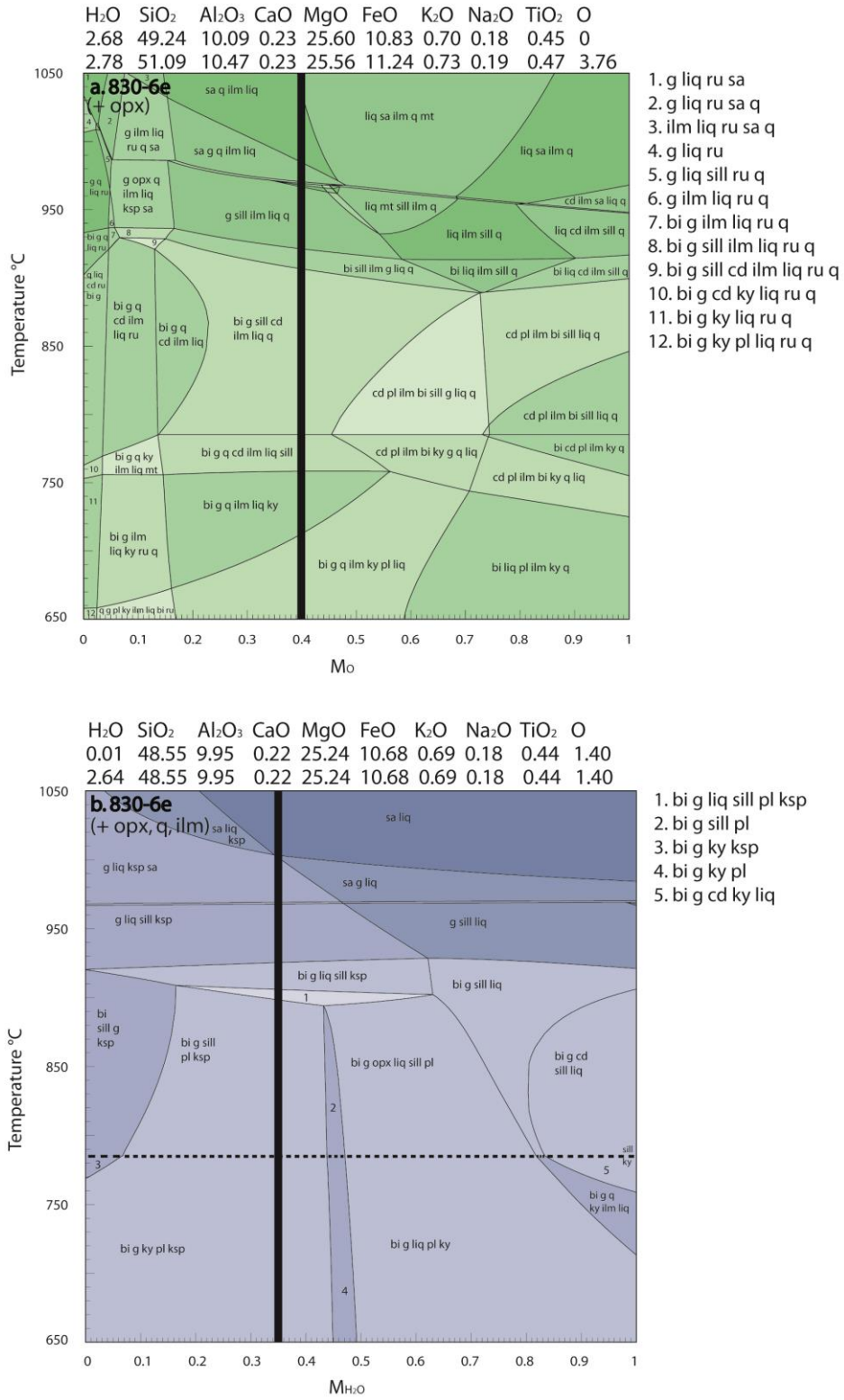

Figure 14: TM_O and TM_{H2O} sections for sample 830-6e with associated composition given in mol %. (a) 830-6e: TM_O represents varying Fe_2O_3 composition with the black line corresponding to the peak assemblage. (b) 830-6e: TM_{H2O} represents varying water content with the black line corresponding to the peak assemblage.

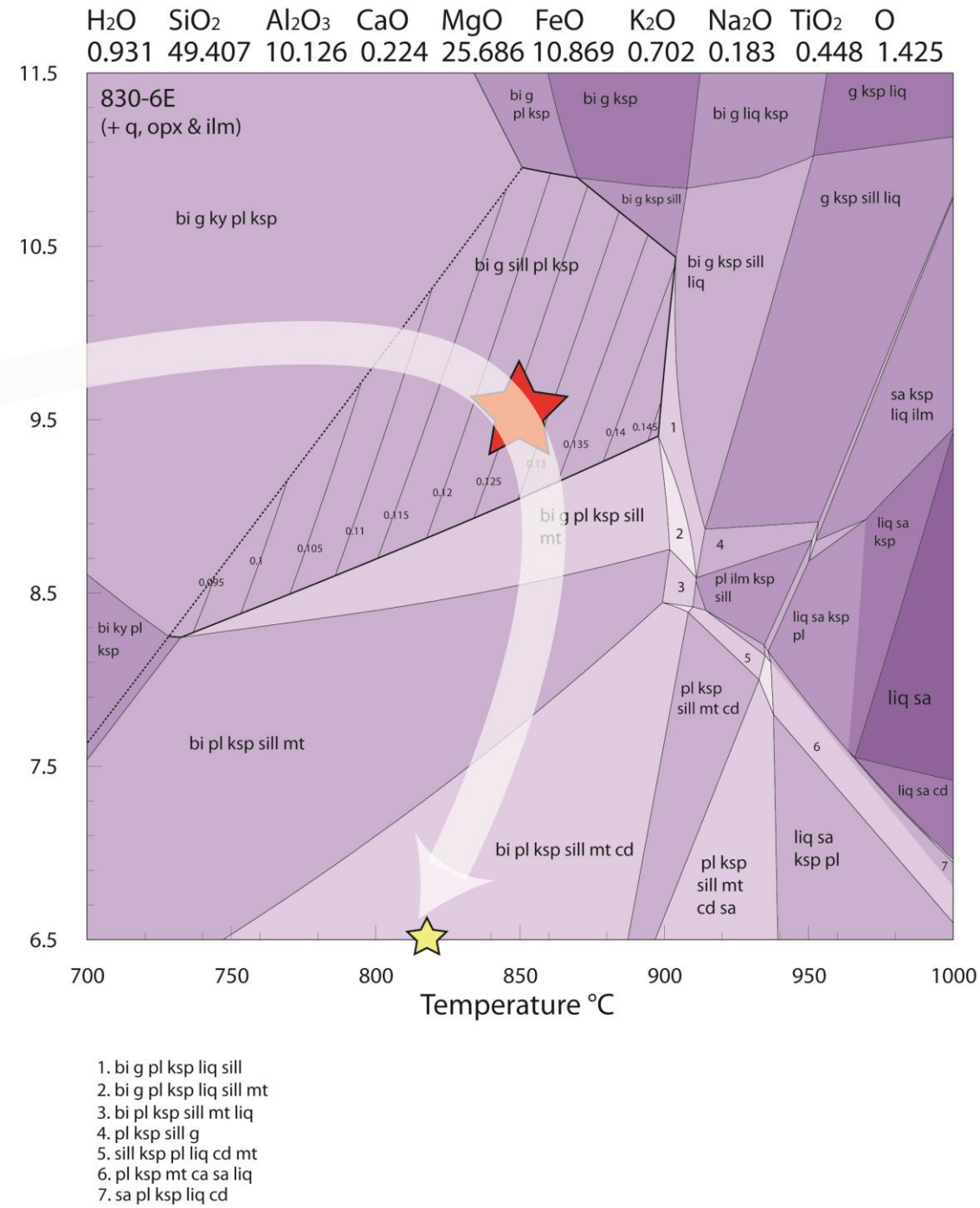

Figure 15: Calculated *P–T* pseudosection for Mg–Al-rich sample 830-6e. The bulk composition is shown above the *P–T* section. The white arrow is the interpreted *P–T* path. The red star in the middle is the interpreted peak temperature assemblage, guided by the Al content in orthopyroxene, and the yellow star represents the peak assemblage of sample 830-14. The bold dashed lines represent the ky–sill reaction boundary.

The T–M_O diagram for 830-14 in Fig. 6a shows that the stability of ilmenite is limited to high ferric iron and lower temperature ranges, magnetite rapidly decreases in the absence of ferric iron and that the stability of garnet is dependant on smaller amounts of ferric iron. The peak assemblage field occurs from approximately M_O = 0.05 to 0.4, and from 600 °C to 800 °C. To continue for the T–M_{H2O} diagram (Fig. 16b) the peak assemblage field (corresponding to M_O = 0.15) was used. On the T–M_{H2O} diagram (Fig. 16b) the peak assemblage occurs towards the higher H_2O range on the diagram, between approximately M_{H2O} = 0.25 to 0.1, and from 750 °C to 800 °C. The peak assemblage field approximately midway (corresponding to M_{H2O} = 0.55) was used for the calculation of the P–T pseudosection.

For sample 830-14 the P–T pseudosection, Fig.17, the peak assemblage fields occurs over the P–T range of 6–8.5 kbar and 800–850 °C. The peak assemblage field is bound up-temperature by the disappearance of magnetite and down-pressure by the introduction of cordierite. The presence of melt abruptly decreases at ~800°C limiting the peak assemblage down-temperature. The peak assemblage is limited to the location of the red star (Fig. 17) by Calcium abundance in garnet (Table 3).

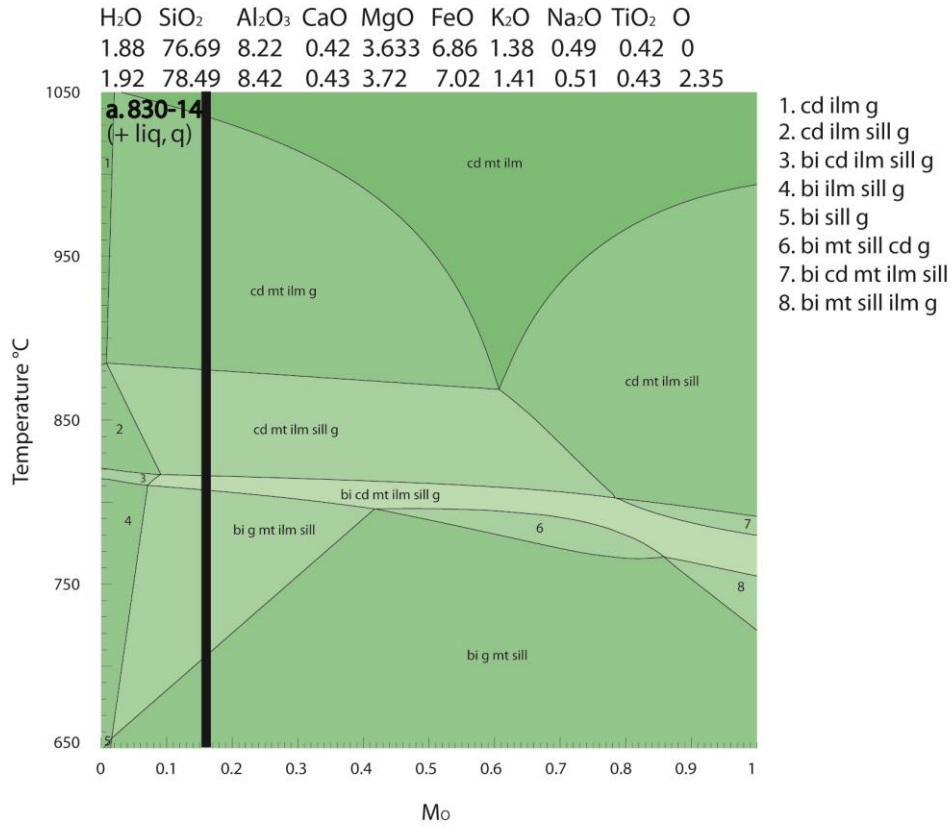

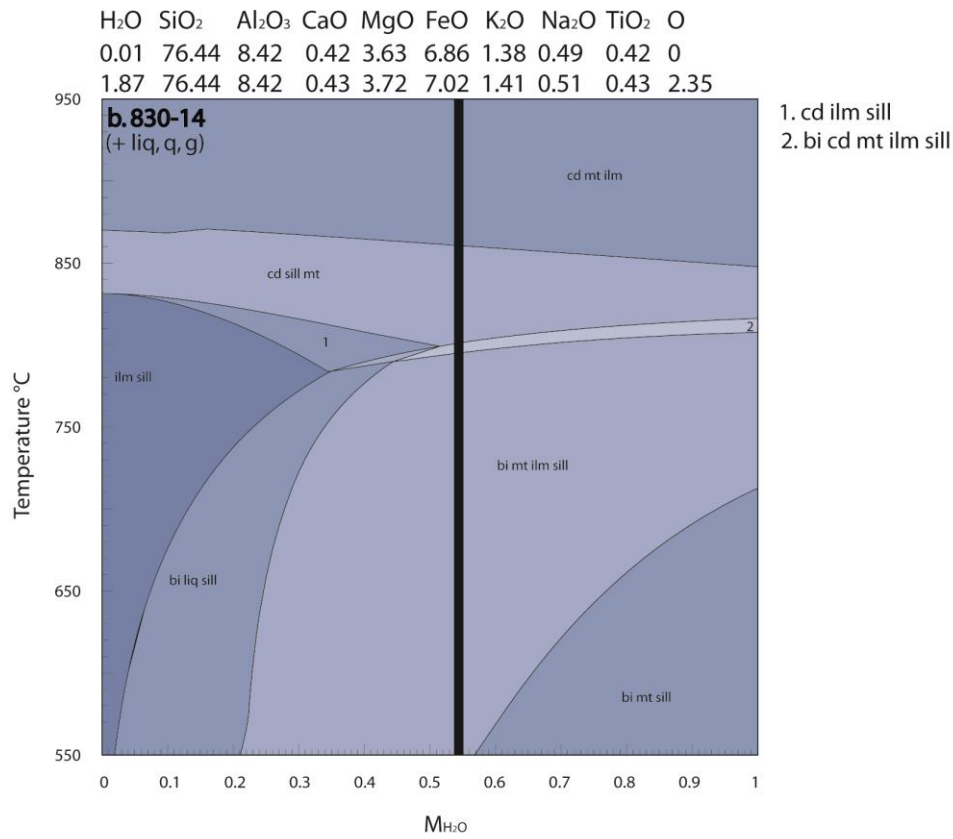

Figure 16: TM_O and TM_{H2O} sections for sample 830-14 with associated composition given in mol %. (a) 830-14: TM_O represents varying Fe_2O_3 composition with the black line corresponding to the peak assemblage. (b) 830-14: TM_{H2O} represents varying water content with the black line corresponding to the peak assemblage.

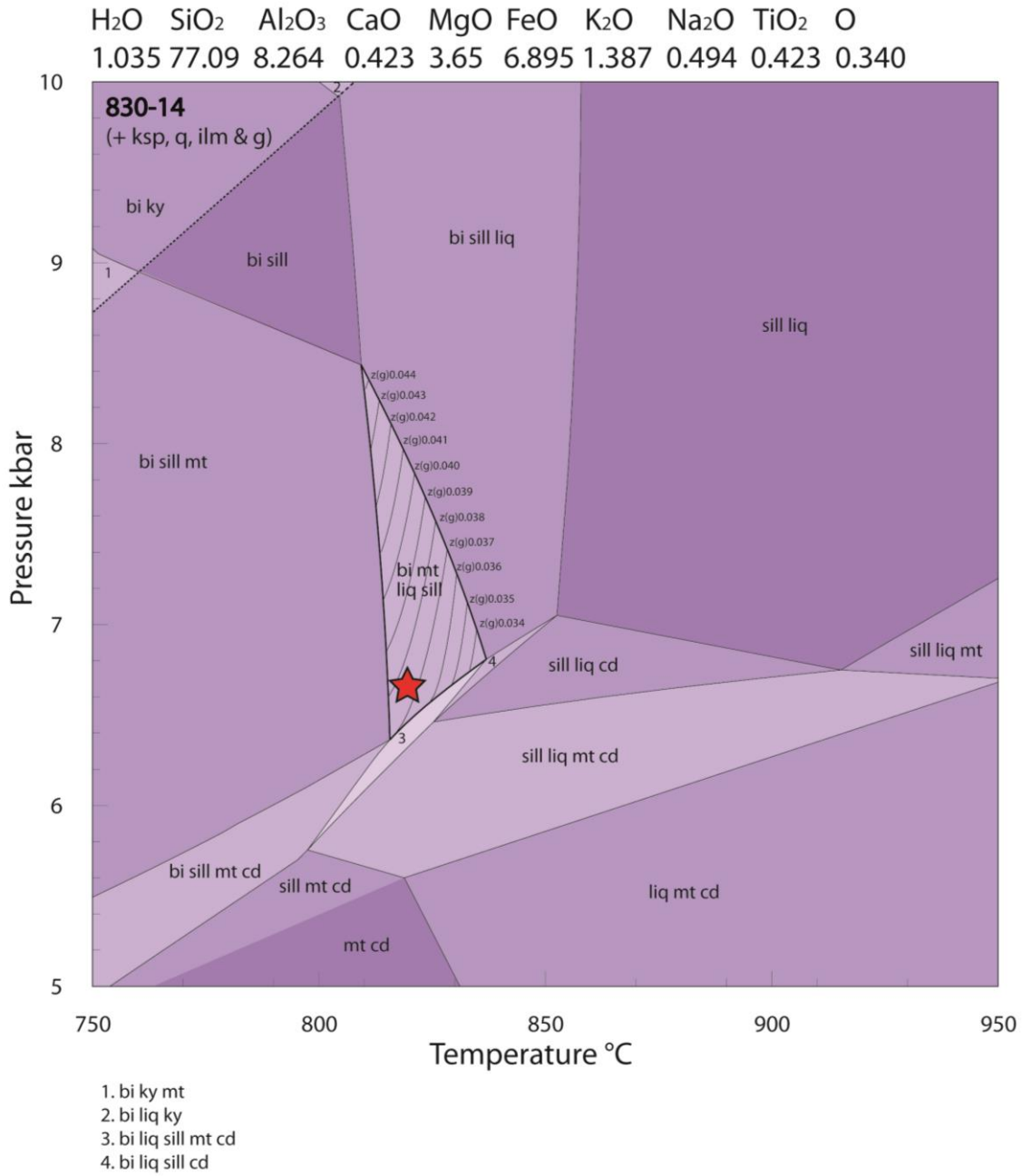

Figure 17: Calculated *P–T* pseudosection for sample 830-14 from the enveloping gneissic and mylonitic domain. The bulk composition is shown above the *P–T* section. The red star in the middle is the interpreted peak temperature assemblage, constrained by the Calcium abundance in garnet. The bold lines represent the alumina-silicate stability fields.

DISCUSSION

Age of metamorphism and deformation

Before discussing the implications of the age data, I will briefly discuss what I interpret the age data to represent. Monazite is a geochronometer that is understood to be reasonably reactive—especially in comparison to zircon—within metamorphic rocks (e.g. Hogdahl et al. 2012; Rubatto et al. 2013), particularly because it rarely survives as a detrital mineral above temperatures of approximately 350 °C (e.g. Janots et al. 2008; Wing et al. 2003). Therefore, in the majority of metamorphic rocks, including the ones in this study, monazite can be interpreted as metamorphic in origin. The age information that monazite preserves can be variously interpreted as either metamorphic, or the result of protracted (re)crystallisation and/or resetting during a long-lived event (e.g. Rubatto et al. 2011; Walsh et al. 2015/in press).

There are two age population distributions, corresponding to the c. 1635–1640 Ma Liebig Orogeny, and c. 1100 – 1200Ma Grenvillian deformation for monazite data found in this study. The most dominant population is the older Liebig Orogeny; recording an event of c. 1630 to 1640Ma metamorphism with limited spread in samples at Hill 830. The spread observed spans ~1540 to ~1620Ma, recorded in samples 830-4A, 830-14 and 830-20E (Fig. 13). This is interpreted to reflect the prolonged deformation in the region, attributed to the longevity of the Chewings Orogeny (Lawson-Wyatt 2012; Morrissey et al. 2014; Walsh et al. 2015/in press). Sample 830-13L records a spectrum of Grenvillian-aged, c. 1100 – c. 1190Ma data.

For samples at Hill 830 a dominant c. 1640 Ma age prevails, previously stated to be resultant of the Liebig Orogeny (Scrimgeour et al. 2005b). The nature of these dates suggests a period of metamorphism with sufficient heat to attain peak *P–T* conditions of 9.5 kbar and ~850 °C (Fig. 15). The presence of c. 1640 Ma ages in sample 830-14 is most probably due to regional c. 1630–1640 Ma metamorphism in the southern Arunta region, as argued by Scrimgeour et al. (2005b) and supported by age data from others (Fields 2012; Lawson-Wyatt 2012; Wong et al. 2015/in press).

The extended spread of 1540-1620Ma ages across samples 830-4A, 830-14 and 830-20E is best explained by the modification of 1640Ma ages, and resetting of monazites by the Chewings Orogeny. The large spread of these dates can be attributed to two factors; 1) the ability of deformation to prolong monazite growth in high temperature rocks after the peak of metamorphism (Kelsey et al. 2003; Morrissey et al. 2014), and 2) that monazite is able to preserve a long record of elevated thermal conditions in the crust (Walsh et al. 2015/in press). In this instance, monazite growth in the c. 1640Ma time frame was continued in the post-peak stage through to ~1613Ma, until resetting select grains by the prolonged Chewings Orogeny. In previous studies Chewings age deformation was scarely recorded from ~1550 to older intervals of ~1600 recorded in the southern Aileron and Warumpi Provinces (Biermeier et al. 2003; Lawson-Wyatt 2012; Scrimgeour et al. 2005b; Wong et al. 2015/in press). In this study it has been dated between intervals of ~1540 and ~1620Ma (Fig. 13), making it's influence across the region compartiable to Chewings scale deformation in the Reynolds Range and Aileron Province (Lawson-Wyatt 2012; Morrissey et al. 2014), although with such a large uncertainty it cannot be unequivocally determined whether the Chewings Event is also long-lived in the Warumpi Province.

The youngest ages recorded in samples 830-13L, 14 and 20E can be accredited to the wide spread Grenvillian-aged event that occurred in the Musgrave Inlier, Albany–Fraser orogen and continued into east Antarctica (e.g. Windmill Islands) (Evins et al. 2010; Kirkland et al. 2011; Morrissey et al. 2011; Smithies et al. 2011; Wong et al. 2015/in press) and that has been documented in other parts of the Warumpi Province (Morrissey et al. 2011; Wong et al. 2015/in press). The presence of Grenvillian-aged metamorphism in the Mt Liebig area of the central Warumpi province is shown conclusively for the first time in this study, thus extending the footprint of this event further west than previously identified (Morrissey et al. 2011; Wong et al. 2015/in press) .

For samples 830-14 and 20E to preserve metamorphic events prior to Grenvillian-aged deformation it may be possible that the temperatures reached at this locality were not high enough to either (a) completely dissolve all pre-existing monazite into melt (Kelsey et al. 2008; Stepanov et al. 2012; Yakymchuk and Brown 2014) and/or (b) overcome the closure temperature for monazite to become open for Pb diffusion (Cherniak et al. 2004).

Pressure-temperature conditions and evolution

As stated earlier, the peak *P–T* conditions for the Mg–Al-rich rocks are one of the two critical pieces of data used by Scrimgeour et al. (2005b) to invoke an accretionary collision event for the Liebig Orogeny. Their *P–T* estimates were based on *P–T* grids and *P–T* pseudosections that were not calculated specifically for the Mg-Al rich granulites. In the presence of silicate melt, the orthopyroxene + sillimanite assemblage is stable at conditions >8.5 kbar and 900 °C (Audibert et al. 1995; Carrington and Harley 1995; Kelsey et al. 2003; Kelsey et al. 2004; White et al. 2001), which represents a crustal depth of ~25–29

km. However, the absence of leucosomes and K-feldspar from outcrop and thin sections of the Hill 830 Mg–Al-rich granulites do not support the presence of melt as part of the peak assemblage. The absence of melt from a granulite facies rock is unusual, as partial melting is typically a critical part of the generation of granulite facies mineral assemblages (e.g. White and Powell 2002). For melt to be absent from a rock at the peak of metamorphism, or indeed absent for most or all of the high-temperature evolution of a granulite facies rock, this must reflect either: (a) that the rocks were previously metamorphosed to high (granulite) conditions and thus previously dehydrated; or (b) the rocks have a sufficiently 'odd' composition that the release of the majority of the hydrous component of the rock was already complete prior to the rocks reaching approximately the normal solidus (~650–700 °C) temperatures for crustal rocks. Although (a) is possible, the absence of ages greater than c. 1640 Ma from the Mg–Al-rich granulites does not support this option. Option (b) is the more likely of the two options as the rocks are unusually poor in silica and potassium. Biotite still exists in the rock, so there is some amount of H_2O in the rock, but the typical reaction for melt production in granulite facies rocks involves, amongst other reactants, the reaction of biotite with quartz (e.g. Peterson and Newton 1989; Vielzeuf and Holloway 1988; Vielzeuf and Montel 1994). If quartz is effectually the limiting reactant during the prograde evolution, then the usual mechanism for biotite to breakdown to produce hydrous melt is no longer feasible (e.g. Harley 1998; McDade and Harley 2001), thus limiting the melt fertility of the rock.

The peak *P*–*T* conditions recorded in sample 830-6E can be constrained within the peak assemblage field in Fig. 15 by the Al content of coarse orthopyroxene (Table 3). The aluminium content of orthopyroxene observed as contours on Fig. 15 is significantly

higher than the aluminium content of sample 830-6E from geochemical analyses, as the contours imply that garnet content is close to 0, which is inconsistent with petrographic interpretations of ~30% (Fig. 15). The variations in results can be potentially be accredited to higher amounts of Fe_2O_3 in the bulk composition or too much Fe_3 partitioned in the a-x model for orthopyroxene (Kelsey et al. 2003).

Therefore, with a detailed analysis the peak *P–T* conditions recorded by the Mg–Al-rich granulites are not arguably less than the estimate of 9–10 kbar and 850°C made by Scrimgeour et al. (2005b). However, there are enough petrographic and field outcrop constraints to delineate the probable *P–T* path for Mg–Al-rich granulites. The prograde part of the *P–T* path is constrained by the interpretation that rectangular aggregates of sillimanite, visible in outcrop as well as thin section, represent pseudomorphing of former andalusite by sillimanite. This evolution from andalusite to sillimanite indicates a high apparent thermal gradient throughout the rocks prograde history. The retrograde part of the *P–T* path is constrained by the development of abundant cordierite and lesser fine-grained orthopyroxene, mostly at the expense of sillimanite and coarse-grained orthopyroxene. The development of cordierite requires that the retrograde part of the *P–T* path follows a decompressive path from peak metamorphic conditions (Fig. 15).

In samples of the enclosing Migmatites the peak assemblage occurs at 6.5kbar and ~800°C. At an outcrop scale the foliated Migmatites have been structurally deformed under prolonged low pressure, high temperature conditions (Figs. 7, 17.) The micro-domain relationships characteristic to this assemblage show monazite lying in the fabric overprinting much of the sample (Fig. 7d), which be interpreted to preserve ages of the

overprinting Grenvillian event. The abundance of cordierite in sample 830-14 is illustrated on Fig. 12, where high manganese rims of garnet and a high abundance of cordierite directly around the central garnet grain strongly suggest the decrease of garnet and increase of cordierite across pressure–temperature space.

Heat source and tectonic implications

The field geology setting as well as the apparent thermal gradient of metamorphism may be used to place constraint on the heat source as well as regional tectonic setting that was responsible for metamorphism of the Mg–Al-rich granulites at c. 1630–1640 Ma. From the peak *P*–*T* conditions, the corresponding apparent thermal gradient is 90 °C kbar^{-1}. This thermal gradient falls within the hotter part of the 'high *T*/*P*' (or Barrovian) realm (Brown 2014; Kelsey and Hand 2015). Apparent thermal gradients of this magnitude are argued by Brown (2006; 2007; 2014) to be the hallmark of Proterozoic collisional orogens. Therefore, at face value the interpretation of a collisional regime by Scrimgeour et al. (2005b) for the Liebig Orogeny is validated. However, if the following aspects are taken into consideration, the interpretation of collisional orogenesis is not necessarily so clear-cut.

As shown on Fig. 3, outcrop of Mg–Al-rich granulites are adjacent to a large 2 km x 1 km gabbro body that is most probably part of widespread mafic–ultramafic intrusions on a scale of hundreds of kilometres throughout the Warumpi and southern Aileron Provinces (Close et al. 2003; Scrimgeour et al. 2005a; Scrimgeour et al. 2005b). Assuming the gabbro at Hill 830 intruded at the time of these other mafic–ultramafic intrusions (i.e. at c. 1630–1640 Ma), the gabbro adjacent to the Mg–Al-rich granulites could provide sufficient

heat to invoke contact metamorphism. However, metamorphism of the Mg–Al-rich granulites probably reflect a much larger-scale tectonic/geodynamic system, argued below, in which case the metamorphism is probably indicative of the thermal character of larger-scale system.

Depositionally, the metasedimentary rocks of the Warumpi Province are poorly constrained; however, Scrimgeour et al. (2005b) report a maximum depositional age of 1661 ± 10 Ma for the Mg-Al rich granulites. The period between the known end of sediment deposition and commencement of the Liebig Orogeny has been suggested to be an indication of rapid burial and exhumation (Close et al. 2003; Scrimgeour 2003; Scrimgeour et al. 2005b). However, that period of time, prior to metamorphism is approximately 10–40 Myr, which is not necessarily an indication that burial of sediments to the deep crust was particularly rapid. Nevertheless, sediment deposition leading up to the c. 1630–1640 Ma period implies a tectonic environment in which a sedimentary basin existed. The presence of a number of igneous intrusions—especially mafic–ultramafic intrusions—in the Warumpi and southern Aileron Provinces (Claoue-Long and Hoatson 2005; Fields 2012; Lawson-Wyatt 2012; Scrimgeour et al. 2005a; Young et al. 1995) at the same time as metamorphism recorded by the Mg–Al-rich granulites, along with the high thermal gradient constrained from the Mg–Al-rich granulites, could instead be argued in favour of an extensional regime, allowing mafic–ultramafic intrusions to penetrate thinned continental crust (Hoatson et al. 2005; Howlett 2012; Pirajna et al. 2008).

Regional implications

The regional interpretation proposed by Scrimgeour at al. (2005b) for the c. 1640Ma timeline was that the exotic Warumpi Province was accreted via subduction-related collision to the southern margin of the NAC. However, periods of parallel magmatism in the southern Aileron and Warumpi Provinces (Anderson 2015; Fields 2012; Lawson-Wyatt 2012), are indicative of an adjacent and simultaneous event. Here I speculatively interpret that in the lead up to, and during the c. 1630–1640 Ma period the Warumpi Province was extended from the NAC. Extension of the southern margin of the NAC (i.e. including Warumpi Province) involved sufficient lithospheric thinning to induce mafic–ultramafic and felsic magmatism at c. 1630–1640 Ma in the southern Aileron and Warumpi Provinces, that included the gabbro at Hill 830 (Fig. 3; Table 2) (Claoue-Long and Hoatson 2005; Fields 2012; Hoatson et al. 2005; Lawson-Wyatt 2012; Pirjina et al. 2008; Scrimgeour et al. 2005a; Wong et al. 2015/in press; Young et al. 1995). The evolution of the NAC over the time period c. 1860–1130 Ma, including the c. 1630–1640 Ma period of interest to this study, is characterised by periods of sedimentation followed by magmatism and/or metamorphism followed by periods of tectonic quiescence (Scrimgeour 2003). A subduction margin to the current-day south of the NAC is stated to control the NAC geology for at least part (or perhaps most) of this time period (e.g. Selway et al. 2009; Selway et al. 2006; Wong et al. 2015/in press; Zhao and McCulloch 1995). The metamorphic style throughout this period is uniformly involving high thermal gradients (Hand and Buick 2001; Scrimgeour 2003; Wong et al. 2015/ in press). This evolutionary pattern has similarities to the long-lived Tasmanides system of eastern Australia, which is classified as an extensional–accretionary orogen (Collins 2002a; Collins 2002b). Extensional–accretionary orogens involve short (<10 Ma) and cyclic shifts from

lithospheric extension to convergence and then back to extension again, related to subduction retreat (periods of extension) vs advance or locking (periods of convergence). Prolonged extension creates ample opportunity for sediment deposition, and also facilitates production of new crust by magmatic activity, interspersed with transient shortening of these hot, thin-crust zones to normal lithospheric thickness during flat subduction (Collins, 2002a; Collins 2002b). Therefore, if this geodynamic framework is applicable, the c. 1630–1640 Ma period investigated in this study may represent either that extension had proceeded far enough to allow magmatism and high thermal gradient metamorphism following a period of sedimentation, or the clockwise *P–T* path retrieved form the Mg–Al-rich granulites could be documenting a transient period of convergence very shortly after extension allowed emplacement of the gabbro and other mafic–ultramafic and felsic magmatic rocks. Therefore, the southern margin of the NAC may be part of a much larger subduction-related, south-migrating, craton-sized extension cycle (Claoue-Long and Hoatson 2005).

CONCLUSIONS

1) Monazite geochronology from Mg-Al rich granulite samples at Hill 830 preserve a c. 5-10Ma period of high-pressure, high-temperature metamorphism at c.1640Ma..
2) The impact of the long-lived Chewings Orogeny on the Warumpi Province was more influential than previously thought, effecting c. 1640 Ma monazite ages.
3) East-west trending Grenvillian-aged deformation continues into the Mount Liebig region of the Warumpi Province, further west than previously documented. This Grenvillian event had pressure temperature conditions of 825°C and 6.5kbar: deficient of impact on the rigid Mg-Al rich granulites.
4) Orthopyroxene and sillimanite are in equilibrium at the peak of metamorphism and become metastable in the post-peak assemblage through the break-down of sillimanite to produce cordierite.
5) Phase equilibria modelling for the melt-deficient, Mg-Al rich granulites at Hill 830 have peak conditions at 850°C and 9.5kbar, progressing into a decompressional post-peak/retrograde path, characteristic of an extensional regime.
6) The gabbro at Hill 830 probably intruded into thinned, extended lithosphere during a coincident period of c. 1630–1640 Ma magmatism between the southern Aileron and Warumpi Provinces, providing sufficient heat to invoke contact metamorphism at Hill 830.
7) That it is argued that the Warumpi Province is not exotic to the Aileron Province and the instance of high-grade, granulite metamorphism found at Hill 830 is not resultant of collisional tectonism during the Liebig Orogeny c. 1635- 1640Ma but of a south-migrating extensional cycle.

ACKNOWLEDGMENTS

Foremost I want to thank my primary supervisor Dr. David Kelsey for his commitment, interest and guidance this year. I have had a fantastic experience throughout this Honours year, aided greatly by your curiosity and insight for my project. Secondly to my co-supervisor Martin Hand, thankyou for your enthusiasm and intellect throughout this year. Thankyou to the postgraduates of the Continental Evolution Research Group- Laura Morrissey, Jade Anderson, Naomi Tucker, Belinda Wong and Kathleen Lane. A special thanks to Laura, for her encouragement and willingness to help with even the smallest of issues. An enormous thankyou to Ben Wade, Aoife McFadden, and the rest of the team at Adelaide Microscropy for their assistance and patience. Katie Howard, for her much appreciated optimism and organisation as Honours Support Officer. To my Honours cohort, thankyou for the much needed sarcasm and cheeriness, its been a pleasure to spend this year with you all. Finally, to my family and friends, I wouldn't have made it through without you and I look forward to seeing you again.

REFERENCES

AUDIBERT N., BERTRAND P. & HENSEN B.J. 1995. Experimental study of phase relations including osumilite in the system K_2O-FeO-MgO-Al_2O_3- SiO_2-H_2O at high pressure and temperature. *Journal of Metamorphic Geology* **13**, 331-344.

ANDERSON J R. 2015. Metamorphic and isotopic characterisation of Proterozoic belts at the margins of the North and West Australian Cratons in time and space. Unpublished PhD thesis, University of Adelaide

BIERMEIER C., STUWE K., FOSTER D. A. & FINGER F. 2003. Thermal evolution of the Redbank thrust system, central Australia: Geochronological and phase-equilbrium constraints. *Tectonics* **22**, 1002.

BROWN M. 2006. Duality of thermal regimes is the distinctive characteristic of plate tectonics since the Neoarchean. *Geology* **34**, 961-964.

BROWN M. 2007. Metamorphic conditions in orogenic belts: a record of secular change. *International Geology Review* **49**, 193-234.

BROWN M. 2014. The contribution of metamorphic petrology to understanding lithosphere evolution and geodynamics. *Geoscience Frontiers* **5**, 553-569.

BUICK I.S., MILLER J.A., WILLIAMS I.S. & CARTWRIGHT I. 2001. Ordovician high-grade metamorphism of a newly recognised late Neoproterozoic terrane in the northern Harts Range, central Australia. *Journal of Metamorphic Geology* **19**, 373-394.

CARRINGTON D.P. & HARLEY S.L. 1995. The stability of osumilite in metapelitic granulites. *Journal of Metamorphic Geology* **13**, 613-625.

CHERNIAK D.J., WATSON E.B., GROVE M. & HARRISON T.M. 2004. Pb diffusion in monazite: a combined RBS/SIMS study. *Geochimica et Cosmochimica Acta* **68**, 829-840.

CLAOUE-LONG J.C. & EDGOOSE C. 2008. The and significance of the Ngadarunga Granite in Proterozoic central Australia. *Precambrian Research* **166**, 219-229.

CLAOUE-LONG J.C. & HOATSON D.M. 2005. Proterozoic mafic-ultramafic intrusions in the Arunta Region, central Australia Part 2: Event chronology and regional correlations. *Precambrian Research* **142**, 134-158.
CLOSE D.F., SCRIMGEOUR I.R., EDGOOSE C.J. & CROSS A. 2004. Late Paleoproterozoic development of the SW margin of the North Australian Craton. *Geological Society if Australia Abstracts* **73**, 149.
CLOSE D., SCRIMGEOUR I., EDGOOSE C., CROSS A. CLAOUE-LONG G., KINNY P. & MEIXNER T. 2003. Redefining the Warumpi Prov ince. *Northern Territory Geological Survery Record* **1**, 1-3.
COLLINS W.J. 2002a. Hot orogens, tectonic switching, and creation of continental crust. *Geology* **30**, 535-538.
COLLINS W.J. 2002b. Nature of extensional accretionary orogens. *Tectonics* **21,** 6-12.
COLLINS W.J. & SHAW R.D. 1995. Geochronological constraints on orogenic events in the Arunta Inlier: a review. *Precambrian Research* **71**, 315-346.
CONNOLLY J.A.D. 2005. Computation of phase equilibria by linear programming: a tool for geodynamic modelling and its application to subduction zone decarbonation. *Earth and Planetary Science Letters* **236**, 524-541.
CONNOLLY J.A.D. & PETRINI K. 2002. An automated strategy for calculation fo phase diagram sections and retrieval of rock properties as a function of physical conditions. *Journal of Metamorphic Geology* **20**, 697-708.
EVINS P.M., SMITIHIES R.H., HOWARD H.M., KIRKLAND C.L., WINGATE M.T.D. & BODORKOS S. 2010. Devil in the detail: the 1150-1100Ma magmatic and structural evolution of the Ngaanyatjarra Rift, west Musgrave Province, central Australia. *Precambrian Research* **183**, 572-588.
FIELDS C. E. 2012. Liebig-aged (ca. 1640Ma) magmatism and metamorphism in ca. 1760Ma crust in the Warumpi and southern Aileron Province, Central Australia: A case for revising the tectonic framework of Proterozoic Australia. B. Sc. (Honours) thesis, Geology and Geophysics, The University of Adelaide, Adelaide (unpubl.)
GOLEBY B.R., SHAW R.D., WRIGHT C., KENNETT B.L.N. & LAMBECK K. 1989. Geophysical evidence for 'thick-skinned' crustal deformation in central Australia. *Nature* **337**, 325-330.
GRIFFIN W.L., BELOUSOVA E.A., SHEE S.R., PEARSON N.J. & O'REILLY S.Y. 2004. Archean crustal evolution in the northern Yilgarn Craton: U-Pb and Hf-isotope evidence from detrial zircons. *Precambrian Research* **131**, 231-282.
HAND M. & BUICK I.S. 2001. Tectonic evolution of th Reynolds-Anmatjire Ranges: a case study in terrain reworking from the Arunta Inlier, central Australia. *Geological Society of London, Specia Publications* **184**, 237-260.
HARLEY S.L. 1988. Proterozoic granulites form the Rauer Group, East Antarctica. I. Decompressional pressure-temperature paths deduced from mafic and felsic gneisses. *Journal of Pertrology* **29**, 1059-1095.
HOATSON D.M., SUN S. & CLAOUE-LONG J.C. 2005. Proterozoic mafic-ultramafic intrusions in the Arunta Region, central Australia: Part 1: Geological setting and mineral potential. *Precambrian Research* **142**, 93-133.
HOGDAHL K., MAJKA J., SJOSTRAM H., PERSSON-WILSSON K.S., CLAESSON S. & KONECHY P. 2012. Reactive monazite and robust zircon growth in diatexites and leucogranites from a hot, slowly cooled orogen; Implications for the Palaeoproterozoic tectonic evolution of central Fennoscandian Shield, Sweden. *Contributions to Mineralogy and Petrology* **163**, 167-188.

HOLLAND T.J.B. & POWELL R. 1998. An internally consistent thermodynamic dataset for phases of petrological interest. *Journal of Metamorphic Geology* **16**, 309-343.
HOLLAND T.J.B. & POWELL R. 2003. Activity-composition relations for phases in petrological calculations: an asymmetric multicomponent formulation. *Contributions to Mineralogy and Petrology* **145**, 492-501.
HOWARD H.M., SMITHIES R.H., KIRKLAND C.L., KELSEY D.E., AITKEN A., WINGATE M.T.D., GROMARD R.Q.D., SPAGGIARI C.V. & MAIER W.D. 2015/in press. The burning heart- The Proterozoic geology and geological evolution of the west Musgrave Region, central Australia. *Gondwana Research*.
HOWLETT D.P. 2012. Geochronological constrains on Yambah and Chewings-aged deformation at Mount Boothby in the south eastern Reynolds Range, central Australia. B. Sc. (Honours) thesis, Geology and Geophysics, The University of Adelaide, Adelaide (unpubl.)
JANOTS E., ENGI M., BERGER J., ALLAZ J., SCHWARZ O. & SPANALER C. 2008. Prograde metamorphic sequence of REE minerals in politic rocks of the Central Alps: implcaitions for allanite stability in Metapelites. *Contributions to Mineralogy and Petrology* **154**, 1-14.
KELSEY D.E. & HAND M. 2015. On ultrahigh temperature crustal metamorphism: phase equilibria, trace element thermometry, bulk composition, heat sources, timescales and tectonic settings. *Geoscience Frontiers* **6**, 311-356.
KELSEY D.E., HAND M., CLARK C. & WILSON C.J.L. 2007. On the application of in situ monazite chemical geochronology to constraining P-T-t histories in high-temperature (>850°C) polymetamorphic granulites from Prydz Bay, East Antarctica. *Journal of the Geological Society* **164**, 667-683.
KELSEY D.E., WHITE R.W., HOLLAND T.J.B. & POWELL R. 2004. Calculated phase equilibria in K_2O-FeO-MgO-Al_2O_3-SiO_2-H_2O for sapphirine-quartz bearing mineral assemblages. *Journal of Metamorphic Geology* **22**, 559-578.
KELSEY D.E., WHITE R.W. & POWELL R. 2003. Orthopyroxene-sillimanite-quartz assemblages; distribution, petrology, quantitative P-T-X constraints and P-T paths. *Journal of Metamorphic Geology* **21**, 439 – 453.
KELSEY D.E., WHITE R.W. & POWELL R. 2005. Calculated phase equilibria in K_2O-FeO-MgO-Al_2O_3-SiO_2-H_2O for silica-undersaturated sapphirine bearing mineral assemblages. *Journal of Metamorphic Geology* **23**, 217-239.
KIRKLAND C.L., SMITHIES R.H., WOODHOUSE A.J., HOWARD H.M., WINGATE M.T.D., BELOUSOVA E.A., CLIFF J.B., MURPHY R.C. & SPAGGIARI C.V. 2013. Constrains and deception in the isotopic record; crustal evolution of the west Musgrave Province, central Australia. *Gondwana Research* **23**, 759-781.
KIRKLAND C.L., SPAGGIARI C.V., PAWLEY M.J., WINGATE M.T.D, SMITHIES R.H., HOWARD H.M., TYLER I.M., BELOUSOVA E.A. & POUJOI M. 2011. On the edge: U-Pb, Lu-Hf, and Sm-Nd data suggests reworking of the Yilgarn Craton margin during formation of the Albany-Fraser Orogen. *Precambrian Research* **187**, 223-247.
KORSCH R., GOLEBY B., LEVEN J. & CRUMMON B. 1988. Crustal architecture of central Australia based on deep seismic reflection profiling. *Tectonophysics* **288**, 57-69.
LAMBECK K., BURGESS G. & SHAW R.D. 1988. Teleseismic travel-time anomalies and deep crustal structure in central Australia. *Geophysical Journal* **94**, 105-124.
LAWSON-WYATT M. 2012. Regional Inkamulla-aged (ca.1740-1755Ma) tectonism along strike of the Mt Hay-Redbank Hill region, southern Aileron Province, central

Australia. B. Sc. (Honours) thesis, Geology and Geophysics, The University of Adelaide, Adelaide (unpubl.)
MCDADE P. & HARLEY S. 2001. A petrogenetic grid for aluminous granulite facies Metapelites in the KFMASH system. *Journal of Metamorphic Geology* **18**, 45-59.
MOELLER A., HENSEN B.J., ARMSTRONG R., MEZGER K. & BALLEVRE M. 2003. U-Pb zircon and monazite age constraints on granulite-facies metamorphism and deformation in the Strangways Metamorphic Complex, central Australia. *Contributions to Mineralogy and Petrology* **145**, 406- 423.
MONTEL., KOMPROBST & VIELZEUF D. 2000. Preservation of old U-Th-Pb ages in shielded monazite: example from the Beni Bousera Hervynian kinzigites (Morocco). *Journal of Metamorphic Geology* **18**, 335-342.
MORRISSEY L., HAND M., RAIMONDO T.. & KELSEY D.E. 2014. Long-lived high-T, low-P granulite facies metamorphism in the Arunta Region, central Australia. *Journal of Metamorphic Geology* **32**, 25-27.
MORRISSEY L., PAYNE H.L., KELSEY D.E. & HAND M. 2011. Grenvillian-aged reworking in the North Australian Craton, central Australia: Constrains from geochronology and modelled phase equilibria. *Precambrian Research.* **191**, 141-165.
PAYNE J.L., HAND M., BAROVICH H.M. & WADE B.P. 2008. Temporal constraints on the timing of high-grade metamorphism in the northern Gawler Craton: implications for assembly of the Australian Proterozoic. *Australian Journal of Earth Sciences* **55**, 623-640.
PETERSON J.Q. & NEWTON R.C. 1989. Reversed experiments on biotite-quartz-feldspar melting in the system KFMASH: implications for crustal anataxis. *Journal of Geology* **97**, 465-485.
PIRAJNA F., MAO J., SHANG A., ZHANG Z. & CHAI F. 2008. The associated of mafic-ultramafic instrusions and A-type magmatism in the Tian Shan and Altay orogens, NW China: Implications for geodynamic evolution and potential for the discovery of new ore deposits. *Journal of Asian Earth Sciences* **32**, 165-183.
RAIMONDO T., HAND M. & COLLINS W.J. 2014. Compressional intracontinental orogens: Ancient and modern perspectives. *Earth-Science Reviews* **130**, 128-153.
RAIMONDO T., CLARK C., HAND M. & FAURE K. 2011. Assessing the geochemical and tectonic impacts of fluid-rock interaction in mid-crustal shear zones: a case study from the intracontinental Alice Springs Orogeny, central Australia. *Journal of Metamorphic Geology* **29**, 821-850.
RUBATTO D. CHAKRABORTY S. & DASGUPTA S. 2013. Time-scales of crustal melting in the higher Himalayan crystallines (Sikkin, Eastern Himalayas) inferred from trace element-constrained monazite and zircon chronology. *Contributions to Mineralogy and Petrology* **165**, 349-372.
RUBATTO D., REGIS D., HERMANN J., BOSTON K., ENGI M., BELTRANDO M. & MCALPINE S.R.B. 2011. Yo-yo subduction recorded by accessort minerals in the Sesia Zone, Western Alps. *Nature Geoscience* **4**, 338-342.
RUBATTO D., WILLIAMS I.S. & BUICK I.S. 2001. Zircon and monazite response to prograde metamorphism in the Reynolds Range, central Australia. *Contributions to Mineral Petrology* **140**, 458-468.
SCRIMGEOUR I.R. 2003. Devloping a revised framework for the Arunta Region. In: Annual Geoscience Exploration Seminar (AGES) 2003. Record of Abstracts, Northern Territory Geological Survery Record 2003-001.

SCRIMGEOUR I.R. 2004. A revised province definition and Palaeoproterozoic framework for the Arunta Region, central Australia. *Geological Society of Australia Abstracts* **73**, 185.
SCRIMGEOUR I., CLOSE D.F. & EDGOOSE C.J. 2005a. *Explanatory Notes, 1: 250 000 Geological Map Series, Mount Liebig SF52-16.* Northern Territory Geological Survey, Darwin.
SCRIMGEOUR I.R., KINNY P.D., CLOSE D.F. & EDGOOSE C.J. 2005b. High-T granulites and polymetamorphism in the southern Arunta Region, central Australia: Evidence for a 1640Ma accretional event. *Precambrian Research* **142**, 1-27.
SELWAY., HAND M., HEINSON G.S. & PAYNE J.L. 2009. Magnetotelluric constraints on subduction polarity: Reversing reconstruction models for Proterozoic Australia. *Geology* **37**, 799-802.
SELWAY K., HEINSON G.S. & HAND M. 2006. Electrical evidence of continental accretion: steeply-dipping crustal-scale conductivity constrast. *Geophysical Research Letters* **33**, 1-4.
SMIT R. 2012. *in prep., October 2012. U-Pb zircon LA-ICP-MS dating, samples NAC-2011-016, NAC-2011-019 & NAC-2011-033*. Hand. University of Adelaide, Adelaide.
SMITHIES R.H., HOWARD H.M., EVINS P.M., KIRKLAND C.L., KELSEY D.E., HAND M., WINGATE M.T.D., COLLINS A.S. & BELOUSOVA E. 2011. High-temperature granulite magmatism, crust-mantle interaction and the Mesoproterozoic intracontinental evolution of the Musgrave Province, central Australia. *Journal of Petrology* **52**, 931-958.
SMITHIES R.H., HOWARD H.M., KIRKLAND C.L., KAHONEN F.J., MEDIN C.C., MAIER W.D., QUENTIN DE GRAMORD R. & WINGATE M.T.D. 2015. Piggy-back supervolcanoes: Long-lived, voluminous, juvenile rhyolite volcanism in Mesoproterozoic central Australia. *Journal of Petrology* **0**, 1-29.
STEPANOV A.S., HERMANN J., RUBATTO D. & RAPP RP. 2012. Experimental study of monazite/melt partitioning with implications for the REE, Th, U geochemistry of crustral rocks. *Chemical Geology* **300-301**, 200-220.
TAYLOR-JONES K. & POWELL R. 2010. The stability of sapphirine + quartz: calculated phase equilibria in FeO–MgO–Al2O3–SiO2–TiO2–O. Journal of Metamorphic Geology **28**, 615-633.
TEYSSIER C., AMRI C. & HOBBS B.E. 1988. South Arunta-Block- the internal zones of a Proterozoic overthust in central Australia. *Precambrian Research* **40**, 157-173.
TUCKER N.M., HAND M. & PAYNE J.L. 2015. A regional rift-relation orogin for medium-pressure, high-temperature metamorphism. *Earth and Planetary Science Letters* **421**, 75-88.
VIELZEUF D. & HOLLOWAY J.R. 1988. Experimental determination of the fluid-absent melting relations in the pelitic system. *Contributions to Minerology and Petrology* **98**, 257-276.
VIELZEUF D. & MONTEL J.M. 1994. Partial melting of metagreywaks. Part 1. Fluid-absent experiments and phase relationshops. *Contributions to Minerology and Petrology* **117**, 375-393.
WALSH A.K., KELSEY D.E., KIRKLAND C.L., HAND M., SMITHIES R.H., CLARK C. & HOWARD H.M. 2015/in press. P-T-t evolution of a large, long-lived, ultrahigh-temperature Grenvillian belt in central Australia. *Gondwana Research.*
WHITE R.W., POWELL R., CLARKE G.L. 2002. The interpretation of reaction textures in Fe-rich metapelitic granulites of the Musgrave Block, central Australia: constraints from

mineral equilibria calculations in the system K2O-FeO-MgO-Al2O3-SiO2-H2O-TiO2-Fe2O3. *Journal of Metamorphic Geology* **20**, 41-55.
WHITE R.W., POWELL R. & HOLLAND T.J.B. 2011. Calculation of partial melting equilibria in the system Na_2O-CaO-K_2O-FeO-MgO-Al_2O_3- SiO_2-H_2O (NCKFMASH). *Journal of Metamorphic Geology* **19**, 139-153.
WHITE R.W., POWELL R., HOLLAND T.J.B. & WORLEY B.A. 2000. The effect of TiO2 and Fe2O3 on metapelitic assemblages at greenschist and amphibolite facies conditions: mineral equilibria calculations in the system K2O-FeO-MgO-Al2O3-SiO2-H2O-TiO2-Fe2O3. *Journal of Metamorphic Geology* ***18***, 497-511.
WING B.A., FERRY J.M. & HARRISON M. 2003. Prograde destruction and formation of monazite and allanite during contact and regional metamorphism of pelites: petrology and geochronology. *Contributions to Mineralogy and Petrology* **145**, 228-250.
WONG B. & MORRISSEY L. 2015. Grenvillian-aged reworking of late Paleoproterozoic crust in the southern Aileron Province, central Australia: implications for the assembly of Mesoproterozoic Australia. PhD thesis, Geology and Geophysics, The University of Adelaide, Adelaide (unpubl.)
YAKYMCHUK C. & BROWN M. 2014. Behavour of zircon and monazite during crustal melting. *Journal of the Geological Society* **171**, 465-479.
YOUNG D.N., FANNING C.M., SHAW R.D., EDGOOSE C.J., BLAKE D.H., PAGE R.W. & CAMACHO A. 1995. U-Pb zircon dating of tectonomagmatic events in the northern Arunta Inlier, central Australia. *Precambrian Research* **72**, 45-68.
ZHAO J.X. & MCCULLOCH M.T. 1988. Geochemical and Nd isotopic systematics of granites from the Arunta Inlier, central Australia: implications for Proterozoic crustal evolution. *Precambrian Research* **71**, 265-299.

APPENDIX A: WHOLE-ROCK GEOCHEMICAL ANALYSIS

	830-5G	830-6E	830-14
Major Elements (wt%)			
SiO2	58.30	49.10	72.10
TiO2	0.70	0.60	0.53
Al2O3	18.63	17.08	13.12
Fe2O3T	10.67	14.35	8.57
MnO	0.09	0.19	0.34
MgO	10.02	17.12	2.29
CaO	0.23	0.21	0.37
Na2O	0.31	0.19	0.48
K2O	1.07	1.10	2.03
P2O5	0.03	0.08	0.05
Total	100.05	100.02	99.88
LOI	0.72	0.80	0.53
Trace and REE (ppm)			
Rb	80.8	82.9	93.9
Sr	11	11	47
Y	14.9	31.7	37.6
Zr	97	87	194
V	108	95	97
Ni	55	41	64
Cr	102	83	147
Nb	5.6	7.4	6.6
Ga	29.0	23.8	27.6
Cu	18	16	40
Zn	189	237	265
Co	42	69	24
Ba	295	189	865
La	23	17	40
Ce	47	52	86
U	<0.5	<0.5	1.1
Th	23.3	24.8	32.8
Sc	10	8	2
Pb	<1	<1	24

APPENDIX B: LA-ICPMS MONAZITE STANDARD ANALYSIS

Analysis No.	Pb207/Pb206	1σ	Pb206/U238	1σ	Pb207/U235	1σ	Conc.	Pb207/Pb206 age	1σ	Pb206/U238 age	1σ	Pb207/U235 age	1σ
MADel													
STDMAD01	0.65723	0.01019	0.08352	0.00111	0.05711	0.00077	104	495.1	29.86	517.1	6.58	512.9	6.24
STDMAD03	0.65215	0.00985	0.08248	0.00109	0.05738	0.00075	101	505.6	28.38	510.9	6.48	509.8	6.05
STDMAD08	0.64911	0.01556	0.08261	0.00121	0.057	0.00135	104	491.1	51.83	511.7	7.18	507.9	9.58
STDMAD10	0.63831	0.01463	0.08088	0.00116	0.05727	0.00129	99	501.6	49.21	501.4	6.94	501.3	9.07
STDMAD11	0.66369	0.01712	0.084	0.00126	0.05734	0.00148	103	504.2	56.2	520	7.47	516.9	10.45
STDMAD12	0.65912	0.02085	0.08313	0.00135	0.05754	0.00185	100	512	69.6	514.8	8.05	514.1	12.76
STDMAD16	0.68671	0.01559	0.08626	0.00125	0.05776	0.00127	102	520.3	47.69	533.4	7.45	530.8	9.39
STDMAD17	0.67908	0.0186	0.08538	0.00132	0.05771	0.00157	101	518.4	58.84	528.2	7.86	526.2	11.25
STDMAD20	0.66065	0.0172	0.08377	0.00129	0.05721	0.00143	103	499.1	54.78	518.6	7.69	515	10.52
STDMAD01	0.69538	0.01132	0.087	0.00127	0.05799	0.00076	101	529.1	28.83	537.8	7.56	536	6.78
STDMAD03	0.65273	0.01007	0.08272	0.0012	0.05726	0.00068	102	501	26.15	512.3	7.16	510.2	6.19
STDMAD04	0.66251	0.01009	0.08422	0.00122	0.05708	0.00066	105	493.9	25.67	521.3	7.27	516.1	6.16
STDMAD08	0.65989	0.01062	0.08314	0.00122	0.0576	0.00073	100	514.3	27.36	514.8	7.28	514.5	6.5
STDMAD08	0.65432	0.01081	0.08327	0.00121	0.05702	0.00078	104	491.7	30.43	515.6	7.19	511.1	6.64
STDMAD10	0.66087	0.0102	0.08326	0.00121	0.05761	0.00069	100	514.5	25.61	515.5	7.2	515.1	6.24
STDMAD13	0.65141	0.01071	0.08264	0.00123	0.0572	0.00074	102	498.6	28.45	511.9	7.3	509.3	6.59
STDMAD13	0.64581	0.00987	0.08221	0.0012	0.05701	0.00066	103	491.3	25.55	509.3	7.15	505.9	6.09
STDMAD15	0.65191	0.01054	0.08243	0.00122	0.05739	0.00072	100	506.2	27.44	510.6	7.27	509.7	6.48
STDMAD16	0.65921	0.01081	0.08354	0.00124	0.05727	0.00074	103	501.3	28.21	517.2	7.39	514.1	6.61
STDMAD17	0.6582	0.01276	0.08345	0.00128	0.05724	0.00096	103	500.2	36.56	516.7	7.6	513.5	7.81
STDMAD38	0.65149	0.01174	0.08269	0.00117	0.05717	0.00093	102	497.7	35.44	512.2	6.94	509.4	7.22
STDMAD39	0.64988	0.01407	0.08235	0.00121	0.05727	0.00118	101	501.5	45.12	510.1	7.2	508.4	8.66
STDMAD41	0.65651	0.01192	0.08353	0.00118	0.05704	0.00094	105	492.4	35.99	517.1	7.01	512.5	7.31
STDMAD43	0.64981	0.01096	0.08215	0.00112	0.05743	0.00094	100	507.7	36.04	508.9	6.65	508.4	6.75
STDMAD44	0.6541	0.01051	0.08319	0.00112	0.05709	0.00088	104	494.3	33.91	515.2	6.66	511	6.45
STDMAD47	0.65267	0.02909	0.08277	0.00172	0.05725	0.00268	102	500.7	100.31	512.6	10.27	510.1	17.87
STDMAD49	0.64369	0.02713	0.08182	0.00164	0.05712	0.00252	102	495.5	95.04	507	9.77	504.6	16.76

Appendix B (continued0

Analysis No.	Pb207/Pb206	1σ	Pb206/U238	1σ	Pb207/U235	1σ	Conc.	Pb207/Pb206 age	1σ	Pb206/U238 age	1σ	Pb207/U235 age	1σ
STDMAD48	0.66781	0.01427	0.08441	0.00124	0.05741	0.00116	103	507	44.12	522.4	7.35	519.4	8.69
STDMAD49	0.64674	0.01407	0.08192	0.00121	0.05729	0.00118	101	502.2	45.17	507.6	7.19	506.5	8.68
STDMAD52	0.671	0.01859	0.08408	0.00133	0.0579	0.00158	98	525.8	58.86	520.4	7.92	521.3	11.29
STDMAD02	0.64962	0.01308	0.08258	0.00145	0.05709	0.00087	103	494.4	33.62	511.5	8.65	508.2	8.05
STDMAD03	0.66515	0.01558	0.08419	0.00153	0.05733	0.00113	103	503.8	43.38	521.1	9.09	517.8	9.5
STDMAD07	0.67439	0.01669	0.08553	0.00169	0.05721	0.00113	106	499.1	42.81	529	10.06	523.4	10.12
STDMAD08	0.63956	0.01615	0.08169	0.00163	0.05681	0.00115	104	483.4	44.58	506.2	9.73	502	10
STDMAD08	0.6501	0.01537	0.08288	0.00165	0.05691	0.00104	105	487.5	40.27	513.3	9.82	508.5	9.46
STDMAD09	0.67363	0.02175	0.08531	0.00182	0.05729	0.0017	105	502.2	64.32	527.8	10.82	522.9	13.19
STDMAD10	0.63688	0.01551	0.08129	0.00163	0.05685	0.00109	103	485.1	42.26	503.8	9.73	500.4	9.62
STDMAD13	0.64467	0.01715	0.08189	0.00169	0.05713	0.00126	102	496	48.36	507.4	10.05	505.2	10.59
STDMAD15	0.66014	0.01818	0.08358	0.00174	0.05732	0.00132	102	503.3	50.44	517.5	10.37	514.7	11.12
STDMAD15	0.65648	0.01651	0.08335	0.0017	0.05715	0.00113	103	497	42.77	516.1	10.12	512.5	10.12
STDMAD16	0.65904	0.01659	0.08368	0.00171	0.05715	0.00113	104	496.8	42.79	518.1	10.17	514	10.15
STDMAD18	0.66207	0.01775	0.08374	0.00174	0.05737	0.00126	105	505.4	47.95	518.4	10.37	515.9	10.84
STDMAD19	0.64266	0.01747	0.08207	0.00171	0.05682	0.00127	105	483.7	48.91	508.5	10.22	503.9	10.8
STDMAD21	0.66886	0.02002	0.08493	0.00183	0.05714	0.00148	105	496.5	56.53	525.5	10.84	520	12.18
STDMAD02	0.65693	0.00945	0.08369	0.00116	0.05696	0.00064	105	489.2	25.04	518.1	6.89	512.7	5.79
STDMAD07	0.65444	0.01136	0.08204	0.00118	0.05787	0.00088	97	524.7	33.12	508.3	7.02	511.2	6.97
STDMAD08	0.71585	0.01117	0.08891	0.00127	0.05841	0.00074	100	545.2	27.47	549.1	7.51	548.2	6.61
STDMAD09	0.65236	0.01057	0.08283	0.00119	0.05714	0.00077	103	496.3	29.6	513	7.09	509.9	6.5
STDMAD11	0.6476	0.00987	0.08229	0.00118	0.05709	0.00069	103	494.4	26.74	509.8	7	507	6.08
STDMAD11	0.65944	0.01002	0.08358	0.00121	0.05725	0.00066	103	500.8	25.34	517.4	7.22	514.3	6.13
STDMAD12	0.66523	0.01036	0.08437	0.00123	0.05721	0.00069	104	499.1	26.53	522.2	7.32	517.8	6.32
STDMAD13	0.65648	0.01042	0.08335	0.00122	0.05715	0.00071	103	496.9	27.33	516.1	7.29	512.5	6.39
STDMAD16	0.64803	0.01084	0.08215	0.00122	0.05725	0.00077	101	500.5	29.46	508.9	7.28	507.3	6.68
STDMAD16	0.6491	0.01023	0.08257	0.00123	0.05705	0.00067	103	492.7	26.11	511.4	7.35	507.9	6.3
STDMAD18	0.65198	0.01035	0.08259	0.00124	0.05728	0.00068	101	502	26.04	511.6	7.38	509.7	6.36
STDMAD20	0.66878	0.01094	0.08486	0.00128	0.05719	0.00071	105	498.2	27.53	525	7.62	520	6.66
STDMAD20	0.65167	0.01016	0.08312	0.00123	0.05689	0.00067	105	486.6	26.21	514.7	7.3	509.5	6.25

Appendix B (continued)

Analysis No.	Pb207/Pb206	1σ	Pb206/U238	1σ	Pb207/U235	1σ	Conc.	Pb207/Pb206 age	1σ	Pb206/U238 age	1σ	Pb207/U235 age	1σ
STDMAD24	0.66179	0.01092	0.08338	0.00124	0.05759	0.00076	100	514	28.97	516.3	7.37	515.7	6.67
STDMAD20	0.67307	0.01366	0.08388	0.00123	0.05823	0.00109	97	537.7	41.04	519.2	7.31	522.6	8.29
STDMAD24	0.64912	0.02081	0.08296	0.00139	0.05686	0.00188	105	485.5	71.88	513.8	8.29	507.9	12.81
STDMAD29	0.65406	0.0109	0.08202	0.0011	0.05795	0.00092	97	527.6	34.65	508.2	6.57	511	6.69
STDMAD28	0.65429	0.02739	0.08236	0.0016	0.05769	0.0025	98	517.8	92.52	510.2	9.51	511.1	16.81
STDMAD29	0.65126	0.0114	0.08199	0.00113	0.05768	0.00093	98	517.3	35.43	508	6.75	509.3	7.01
STDMAD32	0.65216	0.01245	0.08244	0.00116	0.05744	0.00104	100	508.1	39.67	510.7	6.92	509.8	7.65
STDMAD34	0.64682	0.01391	0.08261	0.0012	0.05686	0.00119	105	485.3	45.64	511.7	7.13	506.5	8.58
222													
22201	0.55973	0.01024	0.07198	0.00098	0.05643	0.00096	96	468.6	37.45	448.1	5.89	451.4	6.67
22203	0.55609	0.01092	0.07178	0.00099	0.05622	0.00105	97	460.3	40.98	446.9	5.98	449	7.13
22204	0.5648	0.01211	0.07254	0.00102	0.05649	0.00117	96	470.8	45.57	451.4	6.13	454.6	7.86
22205	0.53923	0.0122	0.07043	0.001	0.05556	0.00123	100	434.7	48.09	438.7	6.04	437.9	8.05
22206	0.54955	0.01985	0.07083	0.00122	0.05631	0.00208	95	463.8	80.7	441.2	7.32	444.7	13.01
22209	0.62989	0.01903	0.07965	0.00128	0.05738	0.00174	97	505.7	65.87	494	7.62	496	11.85
22210	0.59355	0.02154	0.0757	0.00132	0.05688	0.00208	97	486.2	79.54	470.4	7.93	473.1	13.72
22201	0.57081	0.01015	0.07331	0.00109	0.0565	0.00085	97	471.3	33.32	456.1	6.54	458.5	6.56
22202	0.55205	0.00818	0.07148	0.00103	0.05604	0.00062	98	453.7	23.87	445	6.22	446.3	5.35
22203	0.55294	0.00941	0.07203	0.00106	0.05571	0.00078	101	440.3	30.54	448.4	6.39	446.9	6.15
22204	0.56499	0.00875	0.0737	0.00108	0.05563	0.00066	104	437.2	25.83	458.4	6.46	454.8	5.67
22205	0.52237	0.00863	0.06898	0.00102	0.05496	0.00073	104	410.5	29.28	430	6.14	426.7	5.76
22206	0.54846	0.0083	0.07126	0.00102	0.05586	0.00066	100	446.3	25.6	443.7	6.15	444	5.44
22209	0.54799	0.00897	0.07079	0.00104	0.05618	0.00073	97	458.6	28.84	440.9	6.29	443.7	5.88
22221	0.57695	0.01229	0.07486	0.00109	0.05593	0.00113	203	449.1	43.9	465.4	6.56	462.5	7.91
22222	0.55721	0.02508	0.07283	0.00145	0.05552	0.00257	104	433	99.76	453.2	8.72	449.7	16.35
22223	0.58996	0.02472	0.0765	0.00146	0.05597	0.0024	105	450.8	92.93	475.2	8.73	470.8	15.79
22224	0.5585	0.01108	0.07208	0.00104	0.05623	0.00104	98	460.7	40.63	448.7	6.23	450.6	7.22
22226	0.53216	0.03422	0.06928	0.00187	0.05577	0.00378	98	442.8	144.53	431.8	11.26	433.2	22.68
22227	0.55257	0.0276	0.0715	0.0016	0.05611	0.00295	98	456.4	112.84	445.2	9.6	446.7	18.05
22229	0.57307	0.01155	0.07397	0.00107	0.05622	0.00105	200	460.3	41.16	460	6.42	460	7.46

Appendix B (continued)

Analysis No.	Pb207/Pb206	1σ	Pb206/U238	1σ	Pb207/U235	1σ	Conc.	Pb207/Pb206 age	1σ	Pb206/U238 age	1σ	Pb207/U235 age	1σ
22231	0.56758	0.01372	0.07291	0.00111	0.05648	0.00131	97	470.7	51.12	453.7	6.64	456.5	8.88
22201	0.56943	0.0125	0.07299	0.00133	0.0566	0.00099	96	475.4	38.61	454.1	7.97	457.6	8.09
22202	0.56521	0.0132	0.07263	0.00134	0.05645	0.00109	96	469.5	42.55	452	8.06	454.9	8.56
22204	0.56034	0.0139	0.07314	0.00143	0.05558	0.00112	104	435.2	43.87	455.1	8.61	451.7	9.04
22205	0.54523	0.01377	0.07139	0.00141	0.05541	0.00114	104	428.5	44.87	444.5	8.49	441.9	9.05
22209	0.56827	0.01592	0.07378	0.00154	0.0559	0.00133	103	448	51.79	458.9	9.24	456.9	10.31
22210	0.57934	0.02039	0.07515	0.00166	0.05594	0.00182	104	449.8	70.88	467.1	9.96	464	13.11
22211	0.58382	0.01642	0.07564	0.00159	0.05601	0.00133	104	452.3	51.61	470	9.52	466.9	10.53
22212	0.57356	0.0171	0.07462	0.0016	0.05577	0.00144	105	442.9	56.04	463.9	9.59	460.3	11.03
22201	0.56658	0.00827	0.07285	0.00102	0.05643	0.00065	97	468.5	25.44	453.3	6.1	455.8	5.36
22203	0.60815	0.01091	0.07753	0.00112	0.05691	0.0009	99	487.2	34.97	481.4	6.71	482.4	6.89
22204	0.55698	0.00868	0.07266	0.00104	0.05561	0.0007	104	436.6	27.38	452.1	6.23	449.6	5.66
22206	0.58385	0.01122	0.07467	0.00113	0.05674	0.00095	97	480.6	37.16	464.3	6.79	466.9	7.19
22207	0.577	0.01012	0.07429	0.00111	0.05636	0.00082	100	465.9	32.21	462	6.67	462.5	6.52
22208	0.57891	0.00942	0.07504	0.00113	0.05598	0.0007	104	451.4	27.2	466.4	6.76	463.8	6.06
22209	0.58311	0.00925	0.07395	0.00111	0.05722	0.00068	93	499.4	26.15	459.9	6.66	466.5	5.93
22210	0.56441	0.00931	0.07357	0.00111	0.05566	0.00071	105	438.6	27.53	457.7	6.68	454.4	6.04
22211	0.58127	0.00937	0.07491	0.00111	0.0563	0.00071	100	463.6	27.84	465.7	6.66	465.3	6.02
22212	0.58917	0.00984	0.07554	0.00112	0.0566	0.00076	99	475.2	29.72	469.4	6.74	470.3	6.29
22211	0.549	0.01647	0.07114	0.00116	0.05601	0.00167	98	452.5	64.96	443	6.99	444.3	10.8
22216	0.5786	0.05386	0.07432	0.00265	0.05658	0.00555	98	474.4	203.96	462.1	15.88	463.6	34.65
22218	0.55294	0.03767	0.07138	0.00192	0.05625	0.00401	97	461.4	151.33	444.5	11.55	446.9	24.63
22220	0.57622	0.02271	0.07439	0.00138	0.05625	0.00228	100	461.3	88.23	462.6	8.27	462	14.63

APPENDIX C: LA-ICPMS MONAZITE UNKNOWN ANALYSIS

Analysis No.	Location No.	Pb207/Pb206	1σ	Pb206/U238	1σ	Pb207/U235	1σ	Conc.	Pb207/Pb206 age	1σ	Pb206/U238 age	1σ	Pb207/U235 age	1σ
Sample 830-4A (Hill 830)														
UNKNOWN01	3f 1	3.65047	0.06013	0.27429	0.00369	0.09658	0.00146	100	1559.1	28.1	1562.5	18.67	1560.6	13.13
UNKNOWN02	3f 1	4.03798	0.06975	0.29136	0.00398	0.10057	0.00162	100	1634.7	29.69	1648.3	19.89	1641.9	14.06
UNKNOWN03	3f 2	3.73937	0.06623	0.26907	0.0037	0.10085	0.00168	103	1639.9	30.66	1536.1	18.82	1579.8	14.19
UNKNOWN04	3f 2	4.16159	0.17692	0.29509	0.0067	0.10234	0.00461	100	1667	81.12	1666.9	33.37	1666.5	34.8
UNKNOWN05	3f3	4.0144	0.0948	0.28599	0.00444	0.10186	0.00242	101	1658.4	43.33	1621.5	22.24	1637.1	19.2
UNKNOWN06	3f 4	4.00865	0.07358	0.28781	0.00399	0.10108	0.00176	100	1644	32.03	1630.6	19.97	1636	14.92
UNKNOWN07	3f 4	3.4807	0.09466	0.25197	0.00418	0.10025	0.00279	105	1628.7	50.93	1448.6	21.53	1522.9	21.45
UNKNOWN08	3f 5	3.72406	0.11503	0.27062	0.00487	0.09987	0.0032	102	1621.6	58.55	1543.9	24.72	1576.6	24.72
UNKNOWN09	3e 1	3.83223	0.09454	0.28834	0.00462	0.09645	0.00239	98	1556.6	45.73	1633.2	23.13	1599.5	19.87
UNKNOWN10	3e 1	3.53908	0.06921	0.25996	0.00372	0.0988	0.00186	103	1601.6	34.74	1489.6	19.03	1536	15.48
UNKNOWN11	3d 1	3.91142	0.08163	0.28543	0.00421	0.09945	0.00203	100	1613.9	37.52	1618.7	21.12	1616	16.88
UNKNOWN12	3d1	4.44104	0.1238	0.31953	0.00554	0.10087	0.00287	96	1640.2	51.82	1787.5	27.06	1720	23.1
UNKNOWN13	4e 2	3.85259	0.0699	0.29121	0.004	0.09602	0.00164	97	1548.1	31.84	1647.6	19.99	1603.8	14.63
UNKNOWN14	4e 3	3.84602	0.1471	0.27642	0.00592	0.10098	0.00404	102	1642.3	72.54	1573.3	29.88	1602.4	30.82
UNKNOWN15	4e 3	3.80832	0.0949	0.28936	0.00457	0.09552	0.00239	97	1538.3	46.43	1638.4	22.83	1594.5	20.04
UNKNOWN16	4e 4	3.87098	0.07475	0.29166	0.00401	0.09633	0.00179	97	1554.1	34.42	1649.8	20.01	1607.7	15.58
UNKNOWN17	4e 5	3.3672	0.08384	0.24402	0.00383	0.10014	0.00252	106	1626.8	46	1407.6	19.84	1496.8	19.49
UNKNOWN18	4f 1	3.61263	0.09199	0.27171	0.00429	0.09649	0.00248	100	1557.4	47.5	1549.5	21.76	1552.3	20.25
UNKNOWN19	4f 3	3.99648	0.0684	0.29093	0.00393	0.09967	0.00157	99	1617.9	29	1646.2	19.62	1633.5	13.9
UNKNOWN22	5f 1	4.12195	0.09256	0.29754	0.00453	0.10051	0.00221	99	1633.6	40.33	1679.1	22.51	1658.7	18.35
UNKNOWN24	7f 1	4.00037	0.16324	0.29052	0.0063	0.0999	0.00422	99	1622.3	76.66	1644.1	31.46	1634.3	33.15
UNKNOWN28	7f 2	3.92982	0.08548	0.2901	0.00426	0.09827	0.00202	99	1591.6	37.83	1642	21.27	1619.8	17.61
Sample 830-5G (Hill 830)														
UNKNOWN02	8a 9	0.10224	0.00167	0.27093	0.00423	3.81719	0.07119	103	1665.1	29.93	1545.5	21.44	1596.4	15.01
UNKNOWN03	8a 8	0.1007	0.00148	0.27307	0.00416	3.78952	0.06612	102	1637.1	27.12	1556.4	21.08	1590.5	14.02
UNKNOWN04	8a 8	0.09943	0.00117	0.28965	0.00425	3.96897	0.06082	99	1613.5	21.69	1639.8	21.23	1627.9	12.43

Appendix C (continued)

Analysis No.	Location No.	Pb207/Pb206	1σ	Pb206/U238	1σ	Pb207/U235	1σ	Conc.	Pb207/Pb206 age	1σ	Pb206/U238 age	1σ	Pb207/U235 age	1σ
UNKNOWN05	8a 7	0.09986	0.00139	0.29311	0.00442	4.03367	0.06804	99	1621.5	25.67	1657	22.04	1641	13.72
UNKNOWN08	8a 4	0.10106	0.00169	0.29064	0.00456	4.04773	0.07686	100	1643.8	30.69	1644.7	22.79	1643.8	15.46
UNKNOWN09	8a 4	0.09701	0.00112	0.29099	0.00425	3.88989	0.05917	98	1567.4	21.4	1646.5	21.23	1611.6	12.29
UNKNOWN10	8a 4	0.10083	0.0012	0.28805	0.00418	4.00209	0.061	100	1639.4	21.95	1631.8	20.94	1634.6	12.38
UNKNOWN11	8a 5	0.1016	0.0019	0.28882	0.00464	4.0436	0.08252	100	1653.6	34.28	1635.6	23.22	1643	16.61
UNKNOWN12	8b 1	0.1002	0.00129	0.29031	0.00428	4.00815	0.064	100	1627.7	23.73	1643.1	21.37	1635.8	12.98
UNKNOWN13	8b 2	0.10078	0.00137	0.28463	0.00424	3.95271	0.06521	101	1638.6	24.98	1614.6	21.26	1624.5	13.37
UNKNOWN14	8b 2	0.09947	0.00182	0.28494	0.00455	3.90531	0.07877	100	1614.1	33.75	1616.2	22.85	1614.8	16.31
UNKNOWN15	8a 3	0.10032	0.00208	0.29122	0.00486	4.02575	0.08949	100	1630.1	38.13	1647.6	24.27	1639.4	18.08
UNKNOWN16	8a 3	0.09956	0.00121	0.28203	0.00415	3.86916	0.06062	100	1615.9	22.52	1601.6	20.85	1607.3	12.64
UNKNOWN18	8a 3	0.10051	0.00202	0.27865	0.0046	3.85913	0.08376	101	1633.5	36.82	1584.6	23.17	1605.2	17.5
UNKNOWN19	8a 3	0.1014	0.0013	0.29048	0.00432	4.05859	0.06568	100	1649.8	23.53	1643.9	21.56	1646	13.18
UNKNOWN21	8a 2	0.09917	0.00117	0.28353	0.00419	3.87477	0.05997	100	1608.6	21.78	1609.1	21.03	1608.4	12.49
UNKNOWN22	8a 1	0.10037	0.00132	0.28618	0.0043	3.95819	0.06513	100	1630.9	24.28	1622.4	21.57	1625.7	13.34
UNKNOWN23	8a 1	0.10231	0.00121	0.28853	0.00427	4.06789	0.06332	101	1666.5	21.77	1634.2	21.37	1647.9	12.69
UNKNOWN24	9b 4	0.10145	0.00125	0.28889	0.0043	4.03878	0.06409	100	1650.9	22.59	1636	21.5	1642	12.91
UNKNOWN25	9f 2	0.09923	0.00273	0.24542	0.00458	3.35582	0.09389	106	1609.7	50.43	1414.8	23.71	1494.1	21.89
Sample 830-6E (Hill 830)														
UNKNOWN03	19d 2	0.09847	0.00144	0.29105	0.00413	3.94929	0.06555	99	1595.4	26.99	1646.8	20.63	1623.8	13.45
UNKNOWN05	19c 1	0.10267	0.00213	0.28983	0.00456	4.10049	0.08842	101	1673	37.95	1640.7	22.8	1654.4	17.6
UNKNOWN06	19c 1	0.1036	0.00301	0.28775	0.00526	4.10799	0.11779	102	1689.6	52.71	1630.3	26.35	1655.9	23.41
UNKNOWN07	19c 3	0.09841	0.00144	0.29077	0.00413	3.94296	0.06568	99	1594.1	27.14	1645.4	20.63	1622.5	13.49
UNKNOWN08	19c 4	0.1019	0.00179	0.29082	0.00432	4.08358	0.07741	100	1659	32.22	1645.6	21.59	1651	15.46
UNKNOWN09	19c 4	0.09976	0.00147	0.28955	0.00412	3.98039	0.06656	99	1619.6	27.21	1639.3	20.59	1630.2	13.57
UNKNOWN10	19c 5	0.08292	0.00124	0.28862	0.00395	3.29624	0.05123	91	1267.4	28.73	1634.6	19.76	1480.2	12.11
UNKNOWN11	19d 1	0.08351	0.00114	0.28936	0.00388	3.32821	0.0484	91	1281	26.53	1638.3	19.42	1487.7	11.36
UNKNOWN12	19d 2	0.08251	0.00116	0.28998	0.00391	3.29515	0.04899	90	1257.5	27.14	1641.4	19.56	1479.9	11.58
UNKNOWN13	19d 2	0.08119	0.00151	0.28817	0.00418	3.22249	0.06036	90	1226.1	36.09	1632.4	20.9	1462.6	14.51
UNKNOWN15	19d 3	0.08045	0.00103	0.28961	0.00383	3.20893	0.04423	89	1208	24.91	1639.6	19.14	1459.3	10.67

Appendix C (continued)

Analysis No.	Location No.	Pb207/Pb206	1σ	Pb206/U238	1σ	Pb207/U235	1σ	Conc.	Pb207/Pb206 age	1σ	Pb206/U238 age	1σ	Pb207/U235 age	1σ
UNKNOWN16	19d 3	0.0812	0.00116	0.289	0.00391	3.23191	0.04858	90	1226.2	27.79	1636.5	19.57	1464.8	11.66
UNKNOWN17	19d 4	0.08214	0.00114	0.28781	0.00387	3.25605	0.04787	90	1248.9	26.73	1630.6	19.38	1470.6	11.42
UNKNOWN18	19d 5	0.08378	0.00132	0.28865	0.004	3.33087	0.05411	91	1287.4	30.38	1634.8	20.03	1488.3	12.69
UNKNOWN21	18e 1	0.10153	0.0029	0.28963	0.00516	4.05234	0.11521	100	1652.2	52.05	1639.7	25.81	1644.8	23.15
UNKNOWN22	18e 2	0.10241	0.00249	0.29066	0.0048	4.10203	0.10157	101	1668.2	44.32	1644.8	23.96	1654.7	20.21
UNKNOWN24	16d 1	0.10373	0.00274	0.28883	0.00493	4.12879	0.10974	102	1691.8	47.9	1635.7	24.65	1660	21.73
UNKNOWN25	16d 2	0.10353	0.00223	0.28908	0.00449	4.1245	0.09294	102	1688.3	39.3	1636.9	22.48	1659.2	18.42
Sample 830-13L (Enclosing Migmatites)														
UNKNOWN03	1e 1	0.07813	0.00111	0.19761	0.00366	2.12845	0.04303	100	1150.2	28.01	1162.5	19.71	1158.1	13.97
UNKNOWN06	1h 1	0.07899	0.00129	0.19649	0.00375	2.13967	0.04668	100	1172	31.88	1156.4	20.19	1161.7	15.1
UNKNOWN07	1h 2	0.07815	0.00134	0.20084	0.00387	2.16381	0.04875	99	1150.8	33.76	1179.9	20.79	1169.5	15.65
UNKNOWN08	7a 1	0.07687	0.00117	0.19662	0.00389	2.08312	0.04508	99	1117.9	30.06	1157.1	20.95	1143.3	14.85
UNKNOWN09	7a 1	0.07654	0.00117	0.1943	0.00385	2.04954	0.04451	99	1109.2	30.23	1144.6	20.77	1132.1	14.82
UNKNOWN10	7a 2	0.07611	0.00123	0.191	0.00381	2.00343	0.04469	99	1098.1	32.05	1126.8	20.6	1116.7	15.11
UNKNOWN11	7a 3	0.07647	0.00122	0.19412	0.00387	2.04567	0.04543	99	1107.3	31.6	1143.7	20.87	1130.9	15.15
UNKNOWN12	7a 3	0.07552	0.00124	0.1956	0.00391	2.03561	0.04579	98	1082.3	32.5	1151.6	21.07	1127.5	15.32
UNKNOWN13	9a 1	0.07598	0.00137	0.20266	0.0041	2.12193	0.05035	97	1094.6	35.59	1189.6	21.99	1156	16.38
UNKNOWN14	9a 1	0.07642	0.00142	0.19045	0.00387	2.00547	0.0485	99	1106.1	36.75	1123.8	20.97	1117.4	16.39
UNKNOWN15	10a 1	0.07733	0.00123	0.20352	0.00411	2.16886	0.04903	98	1129.7	31.43	1194.2	22.02	1171.1	15.71
UNKNOWN16	10a 1	0.07869	0.00137	0.20128	0.0041	2.18278	0.05142	99	1164.4	34.17	1182.2	22.03	1175.6	16.4
UNKNOWN17	11a 1	0.07819	0.00128	0.19817	0.00402	2.13542	0.04884	100	1151.8	32.09	1165.5	21.61	1160.3	15.82
UNKNOWN18	11a 2	0.07825	0.00148	0.20341	0.00419	2.19357	0.05379	99	1153.2	37	1193.6	22.44	1179	17.1
UNKNOWN20	15a 1	0.07726	0.0014	0.18963	0.00389	2.01913	0.04871	98	1127.9	35.72	1119.4	21.1	1122	16.38
UNKNOWN22	15b 1	0.07682	0.00143	0.19283	0.00397	2.04149	0.04996	99	1116.4	36.68	1136.7	21.47	1129.5	16.68
UNKNOWN23	15b 2	0.07969	0.00171	0.19428	0.00408	2.13377	0.05633	100	1189.3	41.68	1144.5	22.03	1159.8	18.25
UNKNOWN24	15b 3	0.07886	0.00171	0.19282	0.00406	2.09577	0.05587	100	1168.7	42.44	1136.7	21.94	1147.4	18.33
Sample 830-14 (Enclosing Migmatites)														
UNKNOWN02	5f 1	0.10282	0.0017	0.29014	0.00442	4.11223	0.07585	101	1675.7	30.28	1642.2	22.11	1656.7	15.07
UNKNOWN03	5c 1	0.10045	0.00121	0.31271	0.00447	4.32972	0.06541	97	1632.4	22.29	1754	21.93	1699	12.46
UNKNOWN05	9d 2	0.07597	0.00084	0.19993	0.00282	2.09356	0.03029	98	1094.2	22.09	1174.9	15.15	1146.7	9.94

Appendix C (continued)

Analysis No.	Location No.	Pb207/Pb206	1σ	Pb206/U238	1σ	Pb207/U235	1σ	Conc.	Pb207/Pb206 age	1σ	Pb206/U238 age	1σ	Pb207/U235 age	1σ
UNKNOWN06	9d 2	0.07959	0.00086	0.21019	0.00305	2.30547	0.03402	99	1186.8	21.25	1229.8	16.26	1214	10.45
UNKNOWN07	9d 3	0.07632	0.00081	0.19059	0.00276	2.00452	0.02938	99	1103.4	21.18	1124.6	14.97	1117	9.93
UNKNOWN11	9e 1	0.10046	0.00112	0.31221	0.00457	4.32228	0.065	97	1632.6	20.6	1751.6	22.43	1697.6	12.4
UNKNOWN12	9e 1	0.10075	0.00118	0.31235	0.0046	4.33649	0.06688	97	1637.9	21.61	1752.3	22.59	1700.3	12.72
UNKNOWN14	9e 4	0.09567	0.00111	0.30924	0.00454	4.07687	0.06251	95	1541.3	21.57	1736.9	22.37	1649.7	12.5
UNKNOWN15	6c 1	0.08189	0.00102	0.21368	0.00317	2.41118	0.03858	100	1242.8	24.33	1248.4	16.81	1245.9	11.48
UNKNOWN18	10f 1	0.09724	0.00115	0.30442	0.0046	4.07941	0.06454	96	1571.9	22.04	1713.2	22.71	1650.2	12.9
UNKNOWN19	10f 1	0.10249	0.00131	0.3184	0.00487	4.49701	0.07396	97	1669.7	23.45	1781.9	23.79	1730.4	13.66
UNKNOWN20	10f 2	0.10148	0.00185	0.31739	0.00523	4.43895	0.09102	97	1651.5	33.43	1777	25.59	1719.6	16.99
UNKNOWN21	10f 4	0.09942	0.00177	0.31209	0.0051	4.27611	0.08635	96	1613.3	32.8	1751	25.04	1688.8	16.62
UNKNOWN22	10c 1	0.09941	0.00128	0.30539	0.00467	4.18394	0.06919	100	1613.1	23.75	1718	23.04	1670.9	13.55
UNKNOWN23	10c 1	0.10415	0.00175	0.30746	0.00496	4.4132	0.08561	99	1699.4	30.62	1728.2	24.48	1714.8	16.06
UNKNOWN27	10b 3	0.07976	0.00129	0.18897	0.00292	2.07705	0.03883	98	1191.1	31.55	1115.8	15.82	1141.3	12.81
UNKNOWN29	11b 1	0.07902	0.00095	0.21312	0.00315	2.32068	0.03646	100	1172.6	23.65	1245.4	16.75	1218.6	11.15
UNKNOWN30	11b 2	0.08045	0.0012	0.21515	0.00327	2.38537	0.04231	100	1208.1	29.01	1256.2	17.37	1238.2	12.69
Sample 830-20E (Enclosing Migmatites)														
UNKNOWN02	14e 1	0.07458	0.00114	0.20082	0.00287	2.06335	0.03547	96	1057	30.66	1179.7	15.42	1136.7	11.76
UNKNOWN03	14e 2	0.07777	0.00125	0.19396	0.0028	2.07787	0.03698	100	1141	31.59	1142.8	15.12	1141.5	12.2
UNKNOWN04	14d 1	0.09351	0.00225	0.29402	0.00484	3.78719	0.09271	96	1498.3	44.88	1661.6	24.09	1590	19.66
UNKNOWN05	14d 1	0.09695	0.00197	0.20516	0.00317	2.73976	0.05793	111	1566.3	37.59	1203	16.94	1339.3	15.73
UNKNOWN06	14d 2	0.08036	0.00134	0.20506	0.00298	2.26963	0.04117	100	1205.8	32.5	1202.5	15.92	1202.9	12.79
UNKNOWN07	14d 4	0.07462	0.0013	0.20075	0.00293	2.06315	0.03865	96	1058	35	1179.3	15.75	1136.7	12.81
UNKNOWN08	14d 5	0.07406	0.00135	0.19395	0.00286	1.97849	0.03826	97	1043.2	36.28	1142.8	15.43	1108.2	13.04
UNKNOWN09	14c 1	0.08419	0.0015	0.19034	0.0028	2.20717	0.04183	105	1296.9	34.24	1123.2	15.15	1183.3	13.24
UNKNOWN10	14c 1	0.07151	0.00129	0.19776	0.0029	1.94769	0.03734	94	971.9	36.4	1163.3	15.62	1097.7	12.86
UNKNOWN11	14c 2	0.07007	0.00117	0.20924	0.00288	2.01736	0.03498	92	930.4	33.82	1224.8	15.35	1121.4	11.77
UNKNOWN12	14d 2	0.07027	0.00199	0.20435	0.00331	1.97594	0.05502	92	936.3	57.12	1198.6	17.71	1107.3	18.77
UNKNOWN13	14d 2	0.07712	0.00349	0.20286	0.00418	2.15278	0.09395	98	1124.3	87.76	1190.7	22.39	1165.9	30.26
UNKNOWN15	14d 4	0.08838	0.00361	0.31427	0.0067	3.82199	0.14975	91	1390.8	76.35	1761.7	32.87	1597.4	31.53
UNKNOWN17	15c 1	0.08399	0.00279	0.2897	0.00539	3.34809	0.10758	91	1292.2	63.45	1640	26.94	1492.3	25.12

Appendix C (continued)

Analysis No.	Location No.	Pb207/Pb206	1σ	Pb206/U238	1σ	Pb207/U235	1σ	Conc.	Pb207/Pb206 age	1σ	Pb206/U238 age	1σ	Pb207/U235 age	1σ
UNKNOWN20	15c 3	0.09177	0.00161	0.20952	0.00297	2.64586	0.04755	107	1462.6	33.11	1226.3	15.84	1313.5	13.24
UNKNOWN21	15c 4	0.09521	0.00172	0.26792	0.00395	3.51276	0.06641	100	1532.2	33.67	1530.2	20.09	1530.1	14.94
UNKNOWN22	16b 1	0.0753	0.00226	0.18856	0.00326	1.95527	0.05758	99	1076.5	59.12	1113.6	17.67	1100.3	19.78
UNKNOWN23	16b 1	0.07845	0.0024	0.18143	0.00318	1.96013	0.0586	103	1158.3	59.51	1074.8	17.37	1101.9	20.1
UNKNOWN24	16b 2	0.07622	0.00232	0.18271	0.00318	1.91785	0.05717	101	1100.9	59.74	1081.7	17.35	1087.3	19.9
UNKNOWN25	16b 2	0.07558	0.00199	0.18871	0.00308	1.96427	0.05142	99	1084.1	51.99	1114.4	16.7	1103.3	17.61
UNKNOWN26	16b3	0.09988	0.00592	0.29534	0.00878	4.06224	0.22711	99	1621.8	106.46	1668.2	43.71	1646.8	45.55

APPENDIX D: ELEMENTAL MICROPROBE MAPS

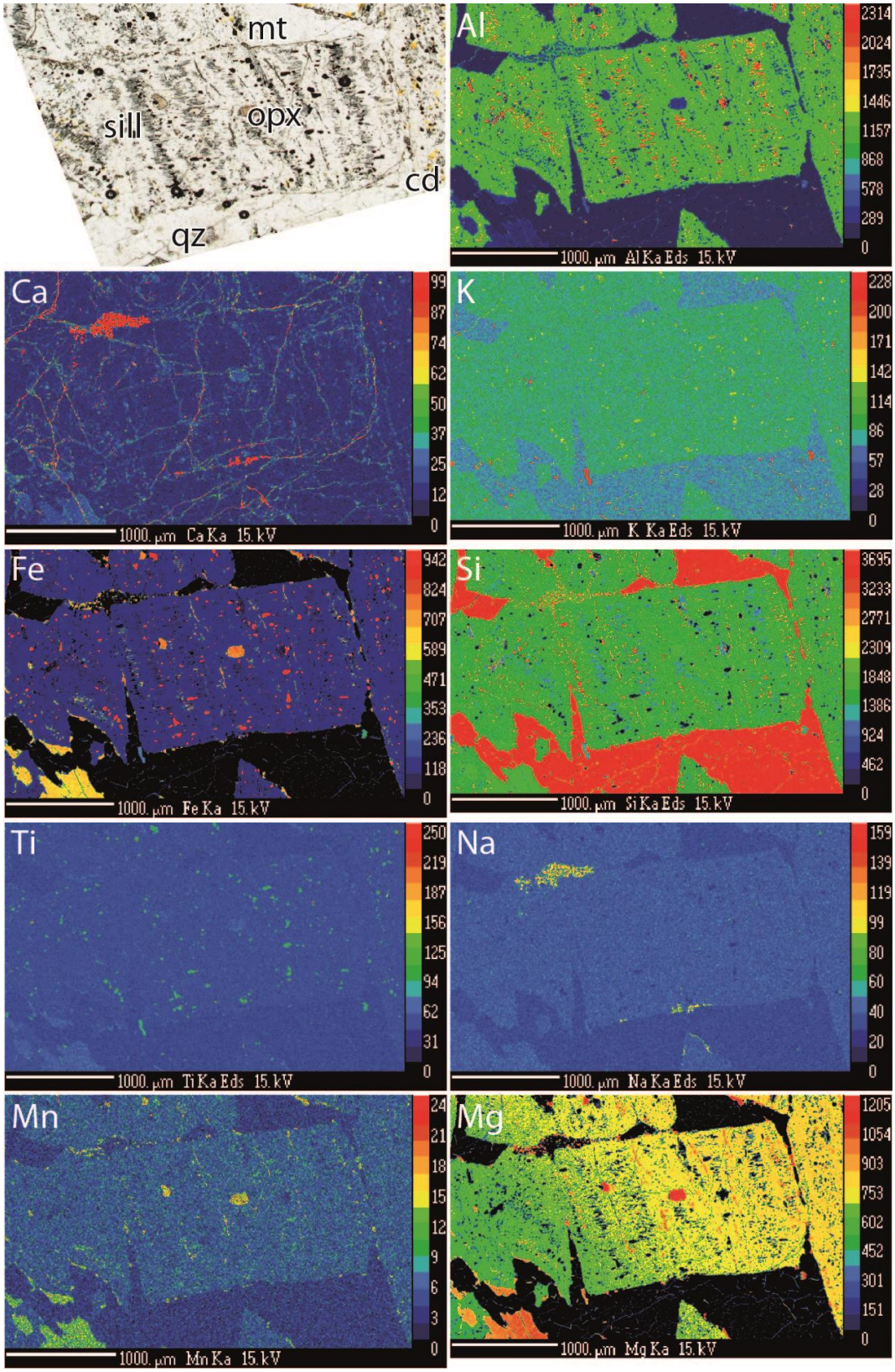

Sample 830-6E: Map B

Appendix D (continued)

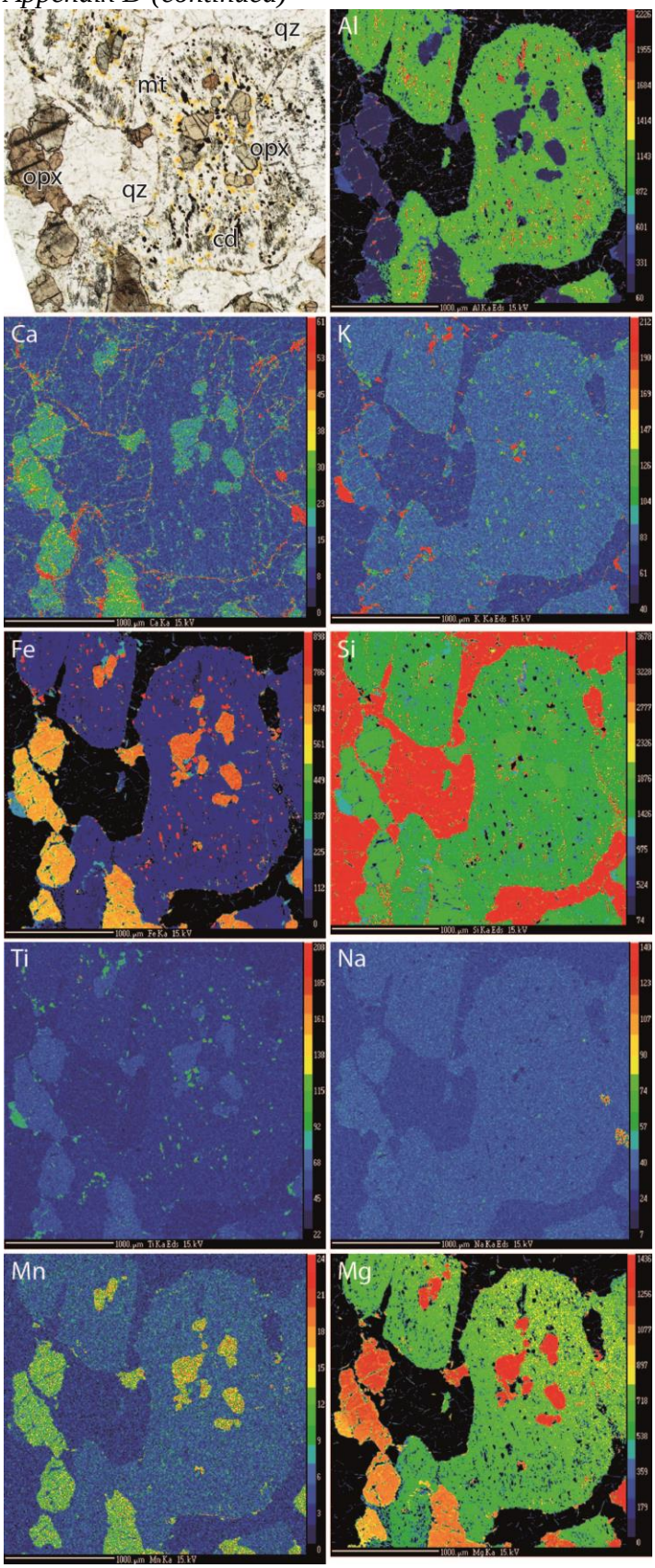

Sample 830-6E: Map C

Appendix D (continued)

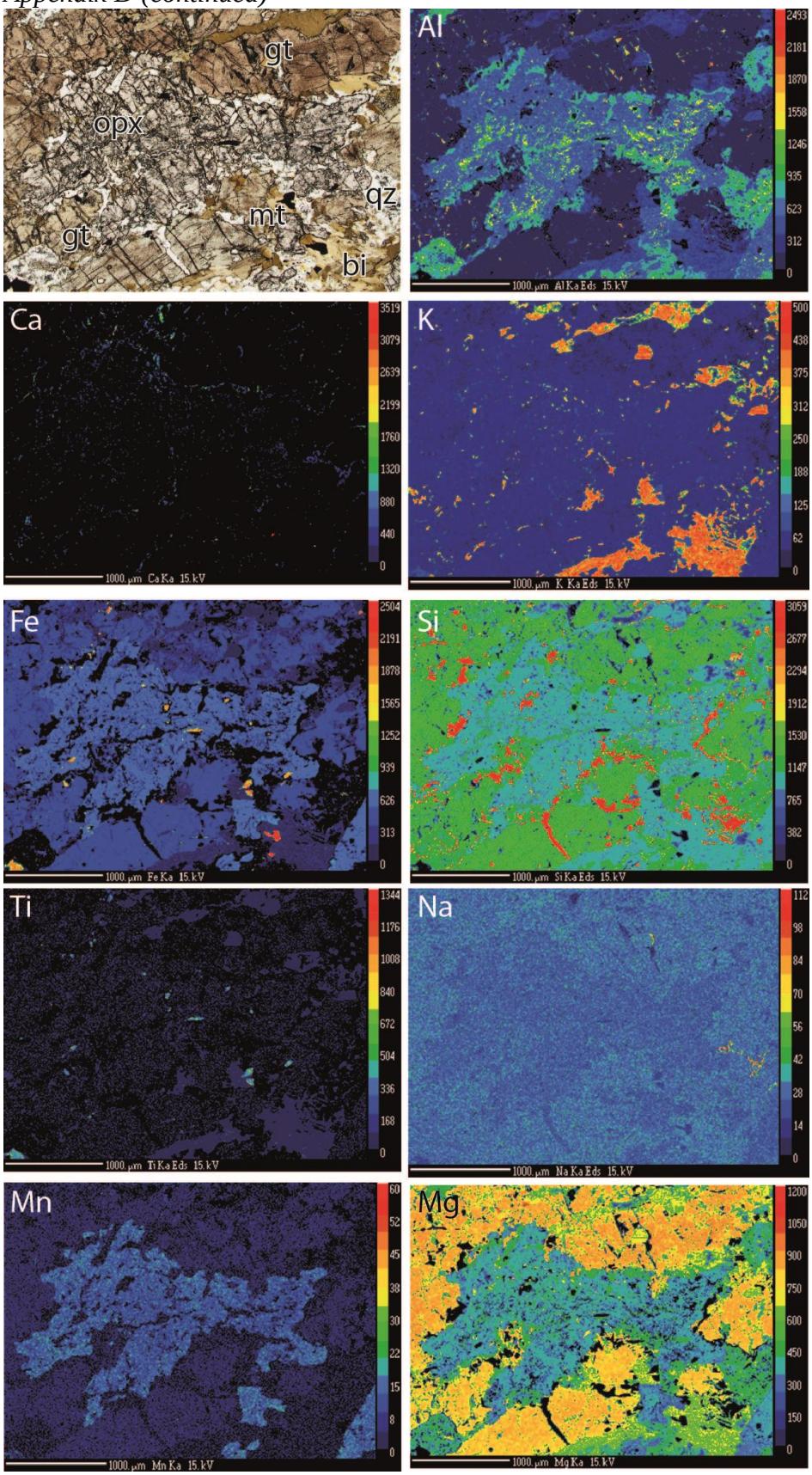

Sample 830-5G: Map A

Appendix D (continued)

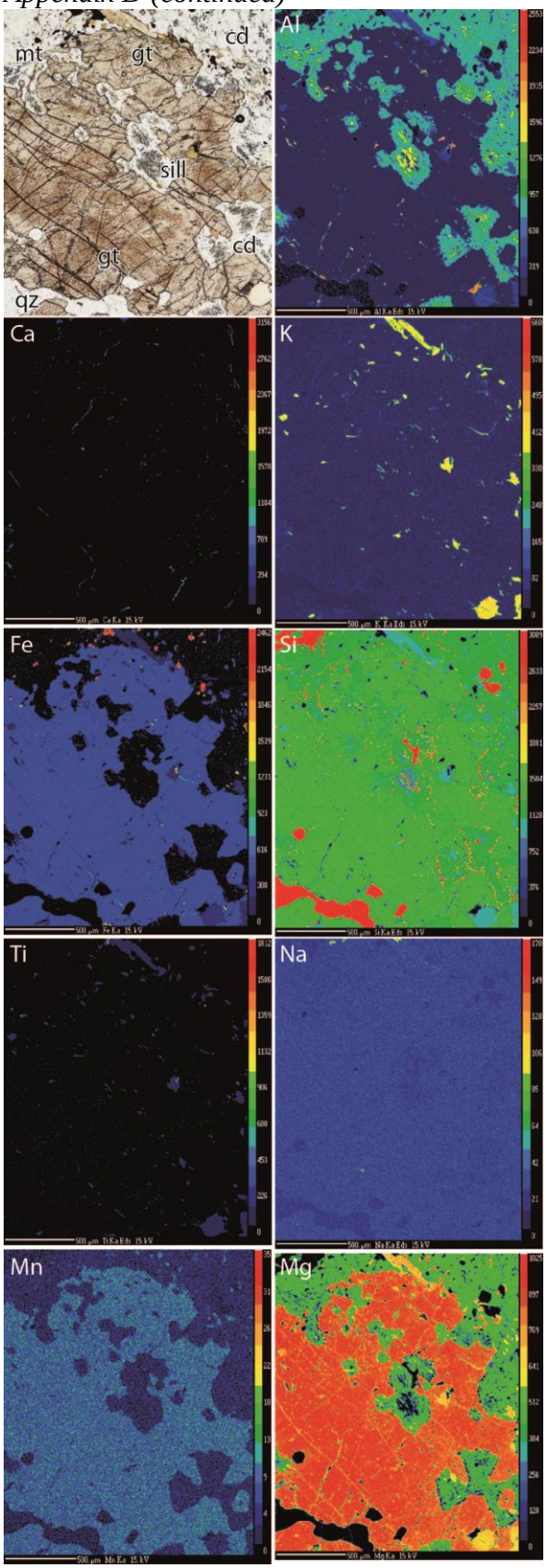

Sample 830-5G: Map C